Extension of the Nonuniform Transformation Field Analysis to linear viscoelastic composites in the presence of aging and swelling

Rodrigue Largenton, Jean-Claude Michel, Pierre Suquet

Extension of the Nonuniform Transformation Field Analysis to linear viscoelastic composites in the presence of aging and swelling.

Rodrigue Largenton[a,*], Jean-Claude Michel[b], Pierre Suquet[b]

[a] *MMC, EDF R&D Site des Renardières, Avenue des Renardières 77818 Moret sur Loing, France, rodrigue.largenton@edf.fr*

[b] *Laboratoire de Mécanique et d'Acoustique, CNRS, UPR 7051, Aix-Marseille Univ, Centrale Marseille, 31, Chemin Joseph Aiguier, 13402 Marseille Cedex 20, France, {michel,suquet}@lma.cnrs-mrs.fr*

Abstract

This study presents a micromechanical modeling by the Nonuniform Transformation Field Analysis (NTFA) of the viscoelastic properties of heterogeneous materials with aging and swelling constituents. The NTFA proposed by Michel and Suquet (2003, 2004) is a compromise between analytical models and full-field simulations. Analytical models, which are available only for specific microstructures, provide effective constitutive relations which can be used in macroscopic structural computations, but often fail to deliver sufficiently detailed information at small scale. At the other extreme, full-field simulations provide detailed local fields, in addition to the composite effective response, but come at a high cost when used in nested Finite Element Methods. The NTFA method is a technique of model reduction which achieves a compromise between both approaches. It is based on the observation that the transformation strains (viscous strains, eigenstrains) often exhibit specific patterns called NTFA modes. It delivers both effective constitutive relations and localization rules which allow for the reconstruction of local fields upon post-processing of macroscopic quantities.

A prototype of the materials of interest here is MOX (mixed oxides), a nuclear fuel which is a three-phase particulate composite material with two inclusion phases dispersed in a contiguous matrix. Under irradiation, its individual constituents, which can be considered as linear viscoelastic, are subject to creep, to aging (time dependent material properties) and to swelling (inhomogeneous eigenstrains). Its overall behavior is therefore the result of the combination of complex and coupled phenomena. The NTFA is applied here in a three-dimensional setting and extended to account for inhomogeneous eigenstrains in the individual phases.

In the present context of linear viscoelasticity the modes can be identified following two procedures, either in each individual constituent, as initially proposed in Michel and Suquet (2003, 2004), or globally on the volume element, resulting into two slightly different models.

For non aging materials, the predictions of both models are in excellent agreement with full-field simulations for various loading conditions, monotonic as well as non proportional loading, creep and relaxation. The model with global modes turns out to be as predictive as the original one with less internal variables. For aging materials, satisfactory results for the

*Corresponding author. Tel: +33 442257382 ; fax: +33 442254747

overall as well as for the local response of the composites are obtained by both models at the expense of enriching the set of modes. The prediction of the global model for the local fields is less accurate but remains acceptable. Use of the global NTFA model is therefore recommended for linear viscoelastic composites.

Keywords: Composite materials, viscoelasticity, aging, model reduction.

1. Introduction

Constitutive relations of solid materials are usually formulated at the engineering, or macroscopic, scale. However, as the loadings become more complex, an accurate description of their response requires the introduction of more internal variables, whose physical meaning is not always clear and for which calibration of more material parameters is needed.

Micromechanical approaches provide an alternative to this phenomenological formulation of macroscopic constitutive relations, based on the observation that all solid materials are heterogeneous at a small enough scale. The present study develops a micromechanically based, reduced model for the effective behavior of linear viscoelastic composites with individual constituents which, in addition to being viscoelastic, undergo aging and swelling. This is typically the case of the nuclear fuel MOX (mixed oxides) under irradiation. Our objective is to predict the effective response of such composites under proportional and nonproportional mechanical loadings as well as under irradiation where aging and swelling play an important role.

Micromechanical models for viscoelastic composites fall, roughly speaking, into one of three categories:

1. *Analytical models.* For viscoelastic composites, the earlier analytical models can be traced back to Hashin (1965) and Laws and Mc Laughlin (1978) where, using, the Laplace transform, the problem is reduced to finding the effective properties of elastic composites with moduli depending on the Laplace parameter. It is now well-known that the effective properties of linear viscoelastic composites with short memory gives rise to long memory effects (Sanchez-Hubert and Sanchez-Palencia, 1978; Suquet, 1987; Barbero and Luciano, 1995). Even when the relaxation spectrum of the individual constituents is discrete (Dirac masses corresponding to a finite number of relaxation times), the effective spectrum of the composite may be a continuous functions with an infinite number of relaxation times (see Rougier et al., 1993; Beurthey and Zaoui, 2000; Masson et al., 2012, among others). Ricaud and Masson (2009) showed that for specific microstructures (two-phase composites whose overall elastic properties are given by one of the Hashin-Shtrikman bounds) the relaxation spectrum of the composites remains discrete. This implies (Ricaud and Masson, 2009; Vu et al., 2012) that the overall constitutive relations of such composites can be alternatively written with a *finite* number of internal variables. Conversely for composites with a continuous relaxation spectrum, an infinite number of internal variables is required and the advantage of an analytical model for subsequent use in a macroscopic numerical computation is lost. This has motivated the introduction of approximate models with a finite number of internal variables (or equivalently with a finite number of relaxation

times) mostly based on the approximation of the continuous relaxation spectrum by Prony series (Rekik and Brenner, 2011; Vu et al., 2012).

The main advantage of the analytical models, exact or approximate, when they require only a finite number of internal variables, is that their use in a numerical simulation is not significantly higher than that of usual linear viscoelastic constitutive relations (obviously this cost depends on the number of internal variables, or relaxation times, in the model). A first limitation of the analytical models for viscoelastic composites is that they make use of the Laplace transform to convert a viscoelastic problem into an elastic one. This procedure does not apply rigorously to aging materials whose material properties depend on time. A second limitation of analytical models is that they only deliver the effective response of the composite and no information about the distribution of the fields (stress, strain) at the microscopic scale, except for the first moment (average) of the fields per phase. The same limitation applies to semi-analytical models based on the inclusion problem (Kowalczyk-Gajewska and Petryk, 2011). However, a more detailed information about the statistics of the fields in the phases (field distribution, intra-phase standard deviation) is often essential to predict the lifetime of structures which is governed by local values of the fields (damage or fracture). An approximation of the statistics of the fields in each phase up to second-order can be obtained by means of the effective internal variable theory of Lahellec and Suquet (2007), Lahellec and Suquet (2013). However this latter approach does not deliver effective constitutive relations and can only be used to obtain the response of the composite to a prescribed loading path.

2. *Full-field simulations.* The response (overall and local) of a representative volume element of the composite can be simulated directly (among many other references, see for instance Michel et al., 1999; Zohdi and Wriggers, 2005; González and Llorca, 2007, for computational micromechanics in general). For linear viscoelastic constituents the unit-cell problem is either solved as an elastic problem after use of the Laplace transform (Yi et al., 1998) or directly by a standard time-integration scheme. The advantage of full-field methods is that they account for all details of the microstructure and provide an accurate (exact to round-off errors) description of the local fields. However, a first limitation of these methods is their computational cost. A second limitation is that full-field simulations provide a constitutive update in a step-by-step time integration, but do not provide a closed form expression for the constitutive relations. And even though the investigation of three-dimensional complex microstructures has become a common practice in the recent years, the coupling between computations at the microscopic scale (material) and at the macroscopic scale (structure) is still the exception, despite the attempts to perform computations at both scales simultaneously through nested Finite Element Methods (FEM^2, see Feyel, 1999; Feyel and Chaboche, 2000).
3. *Reduced-order models.* Reduced models aim at achieving a compromise between the two first class of approaches. On the one hand, they are based on numerical simulations at the microscopic scale (which can sometimes be replaced by analytical calculations) and on the other hand they deliver constitutive relations with a finite number of internal variables which can be used in macroscopic computations, at the expense of certain

approximations which depend on the reduction method. One of the earliest method of this type is the Transformation Field Analysis (TFA) of Dvorak (1992) further developed in Dvorak et al. (1994) and extended to periodic composites by Fish et al. (1997). Assuming uniform eigenstrains within each individual constituent, Fish et al. (1997) derived an approximate scheme which they called, for a two-phase material, the two-point homogenization scheme. The original scheme and this extended scheme have been incorporated successfully in structural computations (Dvorak et al., 1994; Fish and Yu, 2002; Kattan and Voyiadjis, 1993). However, it has been noticed that the TFA induces a spurious kinematic hardening in the effective constitutive relations (Suquet, 1997) and that the application of the TFA to two-phase systems may require, in certain circumstances, a subdivision of each individual phase into several (and sometimes numerous) sub-domains to obtain a satisfactory description of the effective behavior of the composite (Michel et al., 2000; Chaboche et al., 2001; Michel and Suquet, 2003). The need for a finer subdivision of the phases stems from the intrinsic nonuniformity of the plastic strain field which can be highly heterogeneous even within a single material phase. As a consequence, the number of internal variables needed to achieve a reasonable accuracy in the effective constitutive relations, although finite, is prohibitively high. In order to reproduce accurately the actual effective behavior of the composite, it is important to capture correctly the heterogeneity of the plastic strain field.

This last observation has motivated the introduction in Michel et al. (2000), Michel and Suquet (2003) of the Nonuniform Transformation Field Analysis (NTFA) where the (visco)plastic strain field within each phase is decomposed on a finite set of plastic modes which can present large deviations from uniformity. An approximate effective model for the composite can be derived from this decomposition where the internal variables are the components of the (visco)plastic strain field on the (visco)plastic modes. In addition, the NTFA provides localization rules which allow for the reconstruction of local fields upon post-processing of macroscopic quantities and it can predict local phenomena such as the distribution of the plastic dissipation at the microscopic scale (Michel and Suquet, 2009) under cyclic loading. A common feature shared by the TFA and the NTFA is that these methods are applicable in situations where the superposition principle applies, which in practice restrict their range of application to infinitesimal strains.

First applied to two-dimensional situations by Michel and Suquet (2004), the NTFA method has also been implemented in three-dimensional problems by Fritzen and Böhlke (2010) and extended to composites composed of a viscoelastic matrix containing elastic inclusions by Fritzen and Böhlke (2013). By contrast with this latter work, the three phases considered here are all viscoelastic. This opens a new choice for the definition of the modes, which can be defined in each individual constituents or over the whole volume element. Another distinctive feature of the present work is that swelling and aging of the phases are explicitly taken into account.

The paper is organized as follows. Section 2 presents the microstructure of MOX and the behavior of its individual constituents. The NTFA procedure is recalled in section 3 and extended to account for swelling of the constituents. Two possible definitions of the modes,

either defined in each individual phase (as done in Michel and Suquet, 2003) and on the entire volume element are introduced. The accuracy of both models is assessed by comparison with full-field simulations in section 4 for non-aging materials and in section 5 for aging materials.

2. Three-phase particulate composites

Mixed oxide fuel, commonly referred to as MOX fuel, will serve to illustrate the theory developed in this study. It is a nuclear fuel that contains more than one oxide of fissile material, usually consisting of plutonium blended with natural uranium, reprocessed uranium, or depleted uranium (Oudinet et al. , 2008). It is therefore of composite with, roughly speaking, three distinct phases. A brief account on its microstructure and on the behavior of its individual constituents is given here for the reader convenience.

2.1. Microstructure

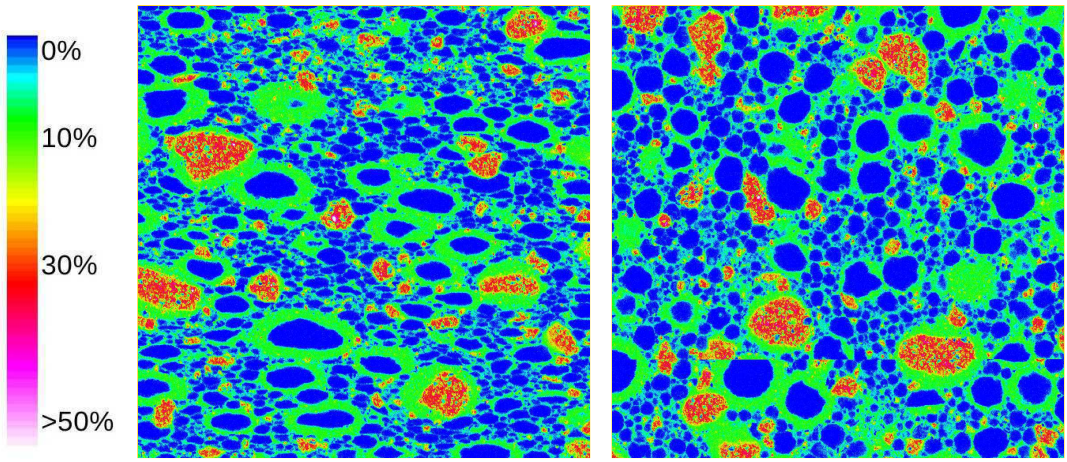

Figure 1: Maps of the Pu concentration in a 1 mm^2 zone of a MOX pellet. (a) Longitudinal cross-section. b) Transverse cross-section.

MOX is a three-phase composite with a connected matrix containing two inclusion phases dispersed in the matrix (Oudinet et al. , 2008). These phases are shown in Figure 1 obtained by electon probe microanalysis (EPMA) where the different colors correspond to different concentrations in plutonium. The three phases can be roughly described as follows:

1. The first inclusion phase (shown in red in Figure 1) is a plutonium rich phase with 25 to 30 % of plutonium in mass. This phase will be referred to as the *Pu clusters*. The swelling of these plutonium clusters under irradiation is quite significant. Their volume fraction in the composite is of the order of 15%. The diameter of Pu clusters varies in the range $[10\mu\text{m}, 70\mu\text{m}]$.

2. The second inclusion phase is a Plutonium poor phase and depleted Uranium rich (shown in blue in Figure 1). Its concentration in plutonium is less than 1 % in mass. It is called the *U clusters*. The swelling of this phase under irradiation is low. Its volume fraction in the composite is of the order of 25%. The diameter of the U clusters is of the order of 30μm.
3. The matrix phase (shown in green in Figure 1) is intermediate between the two other phases, with a moderate concentration in plutonium (typically 6 to 8 % in mass) and with a moderate swelling strain under irradiation.

2.2. Individual constituents

In nominal conditions, the strains remain small and the total strain at a material point $\boldsymbol{x}$ in each of the phases can be decomposed into three contributions:

$$\boldsymbol{\varepsilon}(\boldsymbol{x},t) = \boldsymbol{\varepsilon}_{\mathsf{e}}(\boldsymbol{x},t) + \boldsymbol{\varepsilon}_{\mathsf{v}}(\boldsymbol{x},t) + \boldsymbol{\varepsilon}_{\mathsf{s}}(\boldsymbol{x},t), \tag{1}$$

where $\boldsymbol{\varepsilon}_{\mathsf{e}}$ is the elastic strain, $\boldsymbol{\varepsilon}_{\mathsf{v}}$ is the viscous strain due to creep of the material under irradiation and $\boldsymbol{\varepsilon}_{\mathsf{s}}$ is the eigenstrain (or transformation strain) associated with solid swelling (due to irradiation here, but it could be a consequence of thermal or hygrometric effects in a different context). The elastic strain is related to the Cauchy stress $\boldsymbol{\sigma}$ by the elastic compliance $\boldsymbol{M}$ (inverse of the elastic stiffness $\boldsymbol{L}$):

$$\boldsymbol{\varepsilon}_{\mathsf{e}}(\boldsymbol{x},t) = \boldsymbol{M}^{(r)} : \boldsymbol{\sigma}(\boldsymbol{x},t) \quad \text{when } x \text{ is in phase } r. \tag{2}$$

The creep strain is purely deviatoric and depends on the stress $\boldsymbol{\sigma}$ through a linear relation involving a shear viscosity $G_{\mathsf{v}}^{(r)}$ which is a time dependent scalar, uniform in phase r,

$$\dot{\boldsymbol{\varepsilon}}_{\mathsf{v}}(\boldsymbol{x},t) = \frac{1}{2G_{\mathsf{v}}^{(r)}(t)}\boldsymbol{s}(\boldsymbol{x},t) \quad \text{in phase } r, \tag{3}$$

where $\boldsymbol{s}$ is the stress deviator. The time dependence of the shear viscosity $G_{\mathsf{v}}^{(r)}(t)$ is due to *aging* and is discussed in Appendix C. The swelling strain is isotropic, uniform per phase and depends on irradiation (and therefore is a function of time):

$$\boldsymbol{\varepsilon}_{\mathsf{s}}(\boldsymbol{x},t) = \varepsilon_{\mathsf{s}}^{(r)}(t)\ \boldsymbol{i} \quad \text{in phase } r, \tag{4}$$

where $\boldsymbol{i}$ is the second-order identity tensor. The three phases can be assumed to be isotropic and isotropically distributed in the matrix. To a good level of approximation their elastic moduli can be assumed to be the same. However their viscosity and swelling coefficients differ significantly. For the same applied stress, the creep strains in the Pu clusters are approximately 2.5 times larger than in the matrix where they are 3 times larger than in the U clusters. Similarly the swelling strains in the Pu clusters are 3 times larger than in the matrix where they are 2.5 larger than in the U clusters.

2.3. Reference results by full-field simulations

To the authors' knowledge no complete experimental data are available for the mechanical response of a volume element of irradiated MOX under complex loadings. Most available data pertain to actual pellets where the macroscopic fields (macroscopic strain, temperature) are nonuniform with an unknown spatial distribution. Therefore reference results for the effective response of these three-phase composites under mechanical and irradiation loadings have to be generated using full-field simulations. For this purpose a volume element V of the composite is chosen or generated in such a way that it respects all known statistical information on the microstructure of the material. The response of this volume element to a mechanical and irradiation loading is simulated numerically on a time interval $[0, T]$ by solving the equilibrium and compatibility equations, together with the constitutive relations of the individual phases and appropriate boundary conditions:

$$\left\{ \begin{array}{l} \mathrm{div}(\boldsymbol{\sigma}(\boldsymbol{x},t)) = 0, \quad \boldsymbol{\varepsilon}(\boldsymbol{x},t) = \frac{1}{2}\left(\boldsymbol{\nabla u} + \boldsymbol{\nabla u}^{\mathsf{T}}\right), \\ \boldsymbol{\sigma}(\boldsymbol{x},t) = \boldsymbol{L}(\boldsymbol{x}) : (\boldsymbol{\varepsilon}(\boldsymbol{x},t) - \boldsymbol{\varepsilon}_{\mathsf{s}}(\boldsymbol{x},t) - \boldsymbol{\varepsilon}_{\mathsf{v}}(\boldsymbol{x},t)) \quad , \\ \boldsymbol{\varepsilon}_{\mathsf{s}}(\boldsymbol{x},t) = \displaystyle\sum_{r=1}^{N} \chi^{(r)}(\boldsymbol{x}) \;\; \varepsilon_{\mathsf{s}}^{(r)}(t) \;\; \boldsymbol{i} \quad , \quad \dot{\boldsymbol{\varepsilon}}_{\mathsf{v}}(\boldsymbol{x},t) = \displaystyle\sum_{r=1}^{N} \chi^{(r)}(\boldsymbol{x}) \frac{\boldsymbol{s}(\boldsymbol{x},t)}{2G_{\mathsf{v}}^{(r)}(t)} \\ \boldsymbol{u}(\boldsymbol{x},t) = \overline{\boldsymbol{\varepsilon}}(t).\boldsymbol{x} + \boldsymbol{u}^{*}(\boldsymbol{x},t) \quad , \quad \boldsymbol{u}^{*}(\boldsymbol{x},t) \quad \# \;\; \text{and} \;\; \boldsymbol{\sigma}(\boldsymbol{x},t).\boldsymbol{n}(\boldsymbol{x}) \quad \text{-}\# \quad , \end{array} \right. \tag{5}$$

where $\chi^{(r)}(\boldsymbol{x})$ is the characteristic function of phase r. Periodic boundary conditions are assumed on the boundary of the volume element and this choice is reflected by the periodicity of $\boldsymbol{u}^{*}$ (notation #) and anti-periodicity of $\boldsymbol{\sigma}.\boldsymbol{n}$ (notation -#) on the boundary of V.

The loading is specified by imposing the macroscopic strain path $\overline{\boldsymbol{\varepsilon}}(t)$ and the irradiation history (in other words the history $\varepsilon_{\mathsf{s}}^{(r)}(t)$ in each phase). The effective (or homogenized) constitutive relations relate the overall stress $\overline{\boldsymbol{\sigma}}(t)$ defined as the average of the local stress field

$$\overline{\boldsymbol{\sigma}}(t) = \langle \boldsymbol{\sigma}(\boldsymbol{x},t) \rangle = \frac{1}{|V|} \int_{V} \boldsymbol{\sigma}(\boldsymbol{x},t) \; d\boldsymbol{x},$$

to the history of the overall strain $\overline{\boldsymbol{\varepsilon}}$ and of the swelling strains $\varepsilon_{\mathsf{s}}^{(r)}$. As is well-known (and discussed for instance in Michel et al., 1999), different loading conditions can be considered, for instance by imposing the macroscopic stress history $\overline{\boldsymbol{\sigma}}(t)$, or by imposing the direction of the macroscopic stress and the history of the macroscopic strain in the direction of the macroscopic stress. This latter type of loading, which corresponds for instance to a uniaxial tensile test where the strain the direction of the applied tension is controlled, is best suited for capturing softening effects in the macroscopic response (as it is the case for aging materials) and will be used in the examples of sections 4 and 5.

Generating one, or several, realizations of a "representative volume element" from micrographs of the actual microstructure of the material is an issue by itself. First a software has been developed to process two-dimensional micrographs of the actual material such as those shown in figure 1 and to generate (periodic) artificial three-dimensional microstructures (figure 2).

The main ingredients of the tools developed for this purpose are presented in Largenton et al. (2010) and will not be discussed here in great details. The main steps of the procedure are as follows:

1. First, the two-dimensional micrographs (such as that shown in figure 1) are analyzed: each inclusion phase is segmented according to a procedure described in Oudinet et al. (2008). For each inclusion phase, the surface fraction is determined together with the distribution of diameters in each phase, assuming that each single inclusion can be approximated by a sphere (or a disk).
2. The three-dimensional distribution of diameters of each inclusion phase is deduced from the corresponding two-dimensional distribution by means of standard stereological relations (see Saltykov, 1970, for instance).
3. A realization of the RVE is generated by the Random Sequential Adsorption Algorithm with these data. All spherical inclusions are assumed to be impenetrable with a safety distance 5 μm.
4. Finally the two-point correlation function for each realization is compared to the experimental one. The agreement is observed to be quite good (Largenton et al., 2010).

By contrast with the more elaborate procedure of Lee et al. (2009) where the two-point correlation function is used to define an error between the experimental data and the artificial realization, here the two-point correlation function plays no role in the generation of the realization. However it serves to check *a posteriori* that both two-point correlation functions are in good agreement.

Eight realizations have been generated with the same statistical data namely 15% in volume fraction of Pu clusters with diameter in the range $[10\mu m, 70\mu m]$, matching the experimental distribution of diameters, 25% in volume fraction of U clusters with 30μm in diameter, the volume element being a cube with size $(150\mu\text{m})^3$. Each realization contains 121 Pu clusters of different sizes and 57 U clusters.

A parametric study of the effective response has been performed by a method based on fast Fourier transforms which is a convenient alternative to Finite Elements for volume elements subjected to periodic boundary conditions (Michel et al., 1999). It shows that the ratio between the size of the volume element and that of the inclusions is sufficient to approach stationarity of the effective behavior with a good accuracy. Similarly it has been found that the statistics of the field distribution in the different phases is also almost invariant from one realization to another. Therefore a single realization (shown in figure 2) has been retained in the full-field simulations.

A parametric study of the convergence of the results with respect to the discretization of the volume element has been conducted in parallel. In the FFT method, a realization is an image discretized into equi-sized voxels and the discretization refers to the number of voxels present in the image. Three different discretizations have been considered for a given realization, 75^3, 147^3 and 245^3 voxels, and the response of the volume element to a tension-torsion test (test 1 in section 4) with swelling (but no-aging) has been simulated with the three different

discretizations. The results for the two finer discretizations showed no significant differences and all subsequent simulations were performed with realizations discretized into 147^3 voxels.

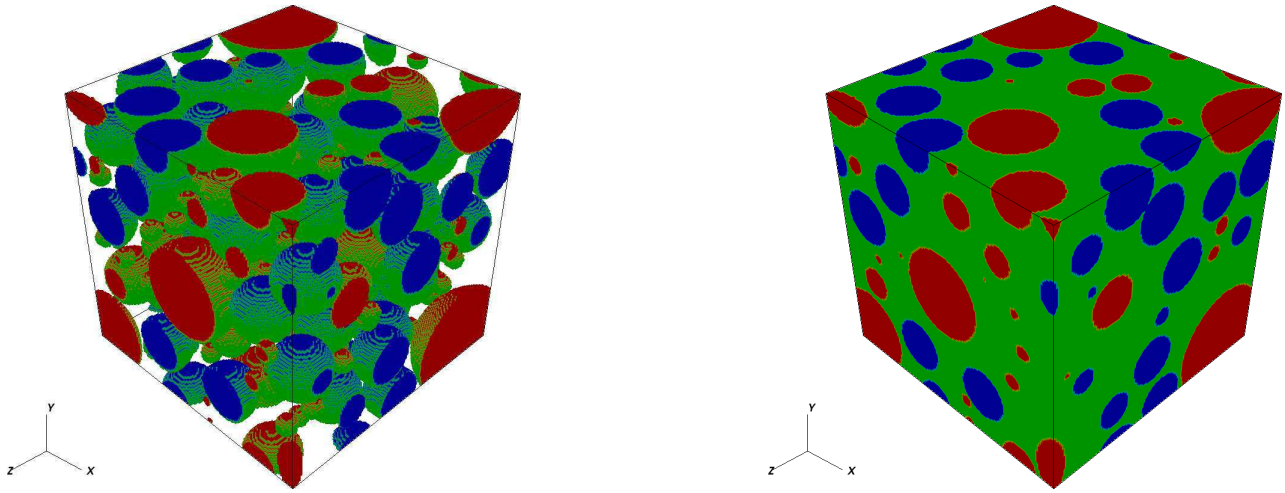

(a) (b)

Figure 2: Periodic realization of a three-dimensional volume element of MOX (discretized into 147^3 pixels). (a) Inclusions only - Pu clusters (in red) U clusters (blue).(b) Entire volume element - matrix (green).

Typical material data for the individual phases used in the full-field simulations can be found in table 1. It should be noticed that the contrast in the swelling strain between the Pu

Phase	E (GPa)	ν (-)	$G_{\mathsf{v}}^{(r)}$ (GPa.s)	$\dot{\varepsilon}_{\mathsf{s}}^{(r)}$ (s^{-1})
Matrix (r=1)	200	0.3	52.94	$7.00E-05$
Pu clusters (r=2)	200	0.3	21.43	$2.10E-03$
U clusters (r=3)	200	0.3	158.83	$2.84E-05$

Table 1: Material data for the individual phases.

clusters and the matrix used in the numerical simulations is artificially larger than in reality (30 instead of 3). This is done on purpose to magnify the effect of the mismatch between the phases.

3. NTFA models

3.1. Nonuniform transformation fields

The basic feature of the NTFA theory (Michel and Suquet, 2003, 2004) is a decomposition of the viscous strain on a set of a few, well-chosen, fields, called *modes*:

$$\boldsymbol{\varepsilon}_{\mathsf{v}}(\boldsymbol{x},t) = \sum_{k=1}^{M} \varepsilon_{\mathsf{v}}^{(k)}(t)\ \boldsymbol{\mu}^{(k)}(\boldsymbol{x})\ , \tag{6}$$

where

- the modes $\left(\boldsymbol{\mu}^{(k)}(\boldsymbol{x})\right)_{k=1,\ldots,M}$ are incompressible tensorial fields ($\mathrm{tr}(\boldsymbol{\mu}^{k})$=0). The choice of these modes is essential in the method and will be discussed in section 3.4.
- the $\left(\varepsilon_{\mathsf{v}}^{(k)}(t)\right)_{k=1,\ldots,M}$'s are the generalized viscous strains associated with each mode for which evolution equations will be derived (section 3.2).

Under the approximation (6), the determination of the field $\boldsymbol{\varepsilon}_{\mathsf{v}}(\boldsymbol{x},t)$ reduces to the determination of the M tensorial variables $\varepsilon_{\mathsf{v}}^{(k)}(t)$. These variables are the *internal variables* of the effective constitutive relations as will be clear from (17). In this sense, the NTFA is a method for model reduction. It should be emphasized that the number of modes M is chosen by the user and is different from N, the number of phases in the composite.

Schematically, the NTFA proceeds in two successive steps:

- *Choice of the modes.* It will be seen in section 3.4 that two strategies are possible, either to define the modes on the entire volume element, or to choose the modes with support in each individual constituent.
- *Evolution equations for the generalized viscous strains.* The evolution equation (3) for the field of viscous strains has to be reduced to a set of differential equations for the generalized viscous strains. These differential equations are derived in section 3.2.

The outcomes are (see section 3.3):

- Explicit constitutive relations relating the overall stress $\overline{\boldsymbol{\sigma}}(t)$ to the overall strain $\overline{\boldsymbol{\varepsilon}}(t)$ and to the generalized viscous strains $\left(\varepsilon_{\mathsf{v}}^{(k)}(t)\right)_{k=1,\ldots,M}$. The macroscopic state variables of the effective constitutive relations are therefore the observable variable $\overline{\boldsymbol{\varepsilon}}$ and the internal variables $\left(\varepsilon_{\mathsf{v}}^{(k)}\right)_{k=1,\ldots,M}$.
- Explicit expressions for the local stress and strain fields $\boldsymbol{\sigma}(\boldsymbol{x},t)$ and $\boldsymbol{\varepsilon}(\boldsymbol{x},t)$ in terms of the state variables $\overline{\boldsymbol{\varepsilon}}$ and $\left(\varepsilon_{\mathsf{v}}^{(k)}\right)_{k=1,\ldots,M}$.

3.2. Reduced variables and evolution equations

Assume that the modes $\boldsymbol{\mu}^{(k)}(\boldsymbol{x})$ have been chosen (this choice is discussed in section 3.4). Then under the decomposition (6), it follows from the superposition principle that the local strain field $\boldsymbol{\varepsilon}$ in the composite can be written as:

$$\boldsymbol{\varepsilon}(\boldsymbol{x},t) = \boldsymbol{A}(\boldsymbol{x}) : \overline{\boldsymbol{\varepsilon}}(t) + \sum_{\ell=1}^{M} (\boldsymbol{D} * \boldsymbol{\mu}^{(\ell)})(\boldsymbol{x}) \;\; \varepsilon_{\mathsf{v}}^{(\ell)}(t) + \sum_{r=1}^{N} (\boldsymbol{D} * \chi^{(r)}\boldsymbol{i})(\boldsymbol{x}) \;\; \varepsilon_{\mathsf{s}}^{(r)}(t) \quad , \tag{7}$$

where $\boldsymbol{A}(\boldsymbol{x})$ is the fourth-order tensorial field of elastic strain localization, $*$ denotes the convolution product, $\boldsymbol{D}(\boldsymbol{x},\boldsymbol{x}')$ is the nonlocal operator expressing the strain at point $\boldsymbol{x}$ resulting

from an eigenstrain at point $\boldsymbol{x}'$. The strain localization tensor $\boldsymbol{A}(\boldsymbol{x})$ and the influence tensors $\left(\boldsymbol{D} * \boldsymbol{\mu}^{(k)}\right)_{k=1,\ldots,M}$, $\left(\boldsymbol{D} * \chi^{(r)}\boldsymbol{i}\right)_{r=1,\ldots,N}$ can be computed once for all by solving $6+M+N$ linear elasticity problems on the RVE (see Appendix B). The corresponding stress field reads as:

$$\begin{aligned}\boldsymbol{\sigma}(\boldsymbol{x},t) = \boldsymbol{L}(\boldsymbol{x}) : \boldsymbol{A}(\boldsymbol{x}) : \overline{\boldsymbol{\varepsilon}}(t) \quad &+ \quad \sum_{\ell=1}^{M} \boldsymbol{L}(\boldsymbol{x}) : \left((\boldsymbol{D} * \boldsymbol{\mu}^{(\ell)})(\boldsymbol{x}) - \boldsymbol{\mu}^{(\ell)}(\boldsymbol{x})\right) \varepsilon_{\mathsf{v}}^{(\ell)}(t) \\ &+ \quad \sum_{r=1}^{N} \boldsymbol{L}(\boldsymbol{x}) : \left((\boldsymbol{D} * \chi^{(r)}\boldsymbol{i})(\boldsymbol{x}) - \chi^{(r)}(\boldsymbol{x})\ \boldsymbol{i}\right) \quad \varepsilon_{\mathsf{s}}^{(r)}(t) \quad .\end{aligned} \tag{8}$$

The *reduced stress* associated with the k-th mode is defined as

$$\tau^{(k)}(t) = \langle \boldsymbol{\mu}^{(k)}(\boldsymbol{x}) : \boldsymbol{\sigma}(\boldsymbol{x},t) \rangle.$$

Using eq. (8), the following relation is obtained:

$$\tau^{(k)}(t) = \boldsymbol{a}^{(k)} : \overline{\boldsymbol{\varepsilon}}(t) + \sum_{\ell=1}^{M} (D^{(k\ell)} - L^{(k\ell)}) \varepsilon_{\mathsf{v}}^{(\ell)}(t) + \sum_{r=1}^{N} (H^{(kr)} - J^{(kr)}) \varepsilon_{\mathsf{s}}^{(r)}(t) \quad . \tag{9}$$

where

$$\left.\begin{aligned} \boldsymbol{a}^{(k)} = \langle \boldsymbol{\mu}^{(k)} : \boldsymbol{L} : \boldsymbol{A} \rangle, \quad D^{(k\ell)} = \langle \boldsymbol{\mu}^{(k)} : \boldsymbol{L} : (\boldsymbol{D} * \boldsymbol{\mu}^{(\ell)}) \rangle, \quad L^{(k\ell)} = \langle \boldsymbol{\mu}^{(k)} : \boldsymbol{L} : \boldsymbol{\mu}^{(\ell)} \rangle, \\ H^{(kr)} = \langle \boldsymbol{\mu}^{(k)} : \boldsymbol{L} : (\boldsymbol{D} * \chi^{(r)}\boldsymbol{i}) \rangle, \quad J^{(kr)} = \langle \boldsymbol{\mu}^{(k)} : \boldsymbol{L} : \chi^{(r)} \ \ \boldsymbol{i} \rangle. \end{aligned}\right\} \tag{10}$$

Using the constitutive equation (3) for the viscous strain-rate, the following relation between the $\tau^{(k)}$'s and the $\varepsilon^{(\ell)}$'s is obtained:

$$\tau^{(k)}(t) = \langle \boldsymbol{\mu}^{(k)}(\boldsymbol{x}) : \boldsymbol{\sigma}(\boldsymbol{x},t) \rangle = \sum_{\ell=1}^{M} V^{(k\ell)}(t) \dot{\varepsilon}_{\mathsf{v}}^{(\ell)}(t), \tag{11}$$

where the incompressibility of the modes has been used and $V^{(k\ell)} = \langle 2G_{\mathsf{v}}\ \boldsymbol{\mu}^{(k)} : \boldsymbol{\mu}^{(\ell)} \rangle$. Conversely

$$\dot{\varepsilon}_{\mathsf{v}}^{(\ell)}(t) = \sum_{m=1}^{M} W^{(\ell m)}(t) \tau^{(m)}(t) \quad \text{where} \quad \boldsymbol{W} = \boldsymbol{V}^{-1}. \tag{12}$$

Taking the time derivative of (9) and using (12), a differential equation for the $\tau^{(k)}$'s is obtained:

$$\dot{\tau}^{(k)}(t) - \sum_{\ell=1}^{M} \sum_{m=1}^{M} (D^{(k\ell)} - L^{(k\ell)}) W^{(\ell m)}(t) \tau_m(t) = \boldsymbol{a}^{(k)} : \dot{\overline{\boldsymbol{\varepsilon}}}(t) + \sum_{r=1}^{N} (H^{(kr)} - J^{(kr)}) \dot{\varepsilon}_{\mathsf{s}}^{(r)}(t) \quad . \tag{13}$$

Therefore the $\tau^{(k)}$'s solve a systems of differential equation of order one where the forcing term is the prescribed history of $\overline{\boldsymbol{\varepsilon}}$ and $\varepsilon_{\mathsf{s}}^{(r)}$. A similar differential system for the $\varepsilon_{\mathsf{v}}^{(k)}$'s can be obtained by means of the relation (12). The history of the internal state variables $(\varepsilon_{\mathsf{v}}^{(k)}(t))|_{k=1,\ldots,M}$ is completely determined by the resolution of these differential equations.

3.3. Effective response and local fields

The local stress and strain field can be expressed in terms of the state variables by means of relations (8) and (7) which can be re-written in a more compact form as:

$$\boldsymbol{\varepsilon}(\boldsymbol{x},t) = \boldsymbol{A}(\boldsymbol{x}) : \overline{\boldsymbol{\varepsilon}}(t) + \sum_{\ell=1}^{M} \boldsymbol{\eta}^{(\ell)}(\boldsymbol{x})\ \varepsilon_{\mathsf{v}}^{(\ell)}(t) + \sum_{r=1}^{N} \boldsymbol{\xi}^{(r)}(\boldsymbol{x})\ \ \varepsilon_{\mathsf{s}}^{(r)}(t)\ \ , \tag{14}$$

and

$$\boldsymbol{\sigma}(\boldsymbol{x},t) = \boldsymbol{L}(\boldsymbol{x}) : \boldsymbol{A}(\boldsymbol{x}) : \overline{\boldsymbol{\varepsilon}}(t) + \sum_{\ell=1}^{M} \boldsymbol{\rho}^{(\ell)}(\boldsymbol{x})\ \varepsilon_{\mathsf{v}}^{(\ell)}(t) + \sum_{r=1}^{N} \boldsymbol{\zeta}^{(r)}(\boldsymbol{x})\ \ \varepsilon_{\mathsf{s}}^{(r)}(t) \tag{15}$$

where

$$\left.\begin{aligned} \boldsymbol{\eta}^{(\ell)}(\boldsymbol{x}) = \boldsymbol{D} * \boldsymbol{\mu}^{(\ell)}(\boldsymbol{x}), \quad \boldsymbol{\xi}^{(r)}(\boldsymbol{x}) = \boldsymbol{D} * \chi^{(r)}\boldsymbol{i}(\boldsymbol{x}), \\ \boldsymbol{\rho}^{(\ell)}(\boldsymbol{x}) = \boldsymbol{L}(\boldsymbol{x}) : \left(\boldsymbol{\eta}^{(\ell)}(\boldsymbol{x}) - \boldsymbol{\mu}^{(\ell)}(\boldsymbol{x})\right), \quad \boldsymbol{\zeta}^{(r)}(\boldsymbol{x}) = \boldsymbol{L}(\boldsymbol{x}) : (\boldsymbol{\xi}^{r}(\boldsymbol{x}) - \chi^{r}(\boldsymbol{x})\boldsymbol{i}). \end{aligned}\right\} \tag{16}$$

Finally the overall stress is obtained by averaging the local stress field (8):

$$\overline{\boldsymbol{\sigma}}(t) = \widetilde{\boldsymbol{L}} : \overline{\boldsymbol{\varepsilon}}(t) + \sum_{k=1}^{M} \langle \boldsymbol{\rho}^{(k)} \rangle\ \varepsilon_{\mathsf{v}}^{(k)}(t) + \sum_{r=1}^{N} \langle \boldsymbol{\zeta}^{(r)} \rangle\ \varepsilon_{\mathsf{s}}^{(r)}(t)\ \ , \tag{17}$$

with (as is classical) $\widetilde{\boldsymbol{L}} = \langle \boldsymbol{L} : \boldsymbol{A} \rangle$.

3.4. Selection of the modes

The choice of the modes plays a key-role in the efficiency of the method. There is no universal choice for these modes and they should rather be chosen according to the type of loading which the structure is likely to be subjected to. This implies that the user should have a rough *a priori* estimate of the domain of variation of the macroscopic strain (or stress), as well as of the intensity of the swelling and of the aging of the phases (variation of the viscous moduli along time). This domain of variation is explored numerically, not in its entirety, but along specific paths, in the same way as an experimentalist would perform uniaxial or multiaxial tests to calibrate a constitutive model. For instance, in the case of swelling, the modes should incorporate information about the response of the volume element under pure swelling of the phases. Similarly if one is interested in the response of the structure under monotonic loading with limited amplitude, the information about the response of the unit-cell will be limited to certain monotonic loading paths in stress space up to a limited amount of deformation. In the absence of such information, standard test should be performed. Given the complexity of the microstructures under consideration, the modes are not determined analytically but numerically from actual viscous strain fields in the unit-cell.

3.4.1. Snapshot method

The modes are selected by the Karhunen-Loève method applied to snaphsots of the viscous strains along certain loading paths. This procedure of selection is sometimes referred to as the Proper Orthogonal Decomposition (POD) snapshot method, widely used in the scientific computing community (pattern recognition, statistical analysis of data....). It seems to have been rediscovered several times under different names (Sirovich, 1987). It is perhaps best known in Fluid Mechanics (Sirovich, 1987; Berkooz et al., 1993; Holmes et al., 1996) and its use in Solid Mechanics is more recent. It was not known to the authors of the first version of the NTFA method (Michel and Suquet, 2003). The POD has been extended in various directions, including the Proper Generalized Decomposition method where the shape functions change with time and are computed on-the-fly (Chinesta et al., 2011; Ladeveze et al., 2010). The simplest version of the Karhunen-Loève method is sufficient here for our purpose.

To keep the loading conditions rather general, monotonic loadings of the volume element are simulated along given directions in the space of overall loadings, consisting of the overall stress $\overline{\boldsymbol{\sigma}}$ and of the swelling of the individual phases. In the present study, 6 purely mechanical loading paths have been defined by loading the volume element along 6 stress "directions" $\boldsymbol{\Sigma}_s^0$ with no swelling of the phases,

$$\overline{\boldsymbol{\sigma}}(t) = \overline{\sigma}(t)\boldsymbol{\Sigma}_s^0, \quad \varepsilon_{\mathsf{s}}^{(r)} = 0 \quad \text{in each phase,} \tag{18}$$

with

$$1 \leq s \leq 3: \quad \boldsymbol{\Sigma}_s^0 = \boldsymbol{e}_s \otimes \boldsymbol{e}_s,$$

and

$$4 \leq s \leq 6: \quad \boldsymbol{\Sigma}_s^0 = \frac{1}{2}\left(\boldsymbol{e}_i \otimes \boldsymbol{e}_j + \boldsymbol{e}_j \otimes \boldsymbol{e}_i\right), \quad s = 9 - i - j,$$

whereas the 7-th test correspond to pure swelling of the phases with no overall stress,

$$\boldsymbol{\Sigma}_7^0 = \mathbf{0}, \quad \dot{\varepsilon}_{\mathsf{s}}^{(r)} \text{ as in Table 1 for each phase.}$$

The first 3 stress directions correspond to uniaxial tension in the three different directions and the next 3 stress directions correspond to pure shear. Numerical simulations are carried out along these paths by increasing monotonically the strain in the direction of the applied stress (except for the loading case 7) up to 10 % deformation along the applied stress for the 6 first loading paths $\overline{\boldsymbol{\varepsilon}} : \boldsymbol{\Sigma}^0 = 10\%$, and up to $t = 10$ s for the 7-th loading path. For the first 6 loading paths the overall strain-rate is fixed $\dot{\overline{\boldsymbol{\varepsilon}}} : \boldsymbol{\Sigma}^0 = 10^{-2}s^{-1}$ so that 10 % deformation is attained in 10 s. The material data used in these simulations can be found in Table 1.

For each loading case $\boldsymbol{\Sigma}^0$, snapshots $\boldsymbol{\theta}^{(k)}|_{k=1,..P}$ of the viscous strain field are saved for further processing at different values of the strain $\overline{\boldsymbol{\varepsilon}} : \boldsymbol{\Sigma}^0$ along the applied stress $\boldsymbol{\Sigma}^0$. These snapshots are normalized *i.e.* divided by $\langle\theta_{eq}^{(k)}\rangle$ where $\theta_{eq} = \left(\frac{2}{3}\theta_{ij}\theta_{ij}\right)^{1/2}$ (recall that the viscous strains are incompressible). At the end of each simulation of a given loading case, P snapshots are stored (and normalized). In the present study, the snapshots are stored every 0.4 s and therefore $P = 25$ (each test lasts 10 s).

The actual modes are then extracted from these snapshots by means of the *Karhunen-Loève* (K-L) transform (or Proper Orthogonal Decomposition) which is well documented in the literature (see for instance Holmes et al., 1996).

First the $P \times P$ correlation matrix between the snapshots for the same loading path is formed

$$g^{(k\ell)} = \langle \boldsymbol{\theta}^{(k)}(x) : \boldsymbol{\theta}^{(\ell)}(x) \rangle, \quad k, \ell = 1, \ldots, P,$$

and its eigenvalues $\lambda^{(k)}$ and eigenvectors $\boldsymbol{v}^{(k)}$ are computed. The actual modes are expressed as a combination of the eigenvectors as

$$\boldsymbol{\mu}^{(k)}(x) = \sum_{\ell=1}^{P} v_\ell^{(k)} \boldsymbol{\theta}^{(\ell)}(x) \quad . \tag{19}$$

Note that the modes, as the eigenvectors of the symmetric matrix $\boldsymbol{g}$, are orthogonal to each other. Another well-known feature of the K-L transform is that the quantity of relevant information (its correlation with the set of snapshots) contained in an eigenvector $\boldsymbol{v}^{(k)}$ is expressed by the magnitude of the corresponding eigenvalue $\lambda^{(k)}$. This property can be used to truncate the set of modes, retaining the most relevant ones. Ordering the eigenvalues in decreasing order, the M modes corresponding to the largest eigenvalues can be selected by applying a threshold criterion

$$\sum_{k=1}^{M} \lambda^{(k)} / \left(\sum_{k=1}^{P} \lambda^{(k)} \right) \geq \alpha,$$

In the present study $\alpha = 0.9999 = 1 - 10^{-4}$.

A first application of the K-L transform is performed with the snapshots corresponding to the same loading path. The resulting modes are mutually orthogonal, but not necessarily orthogonal to the modes corresponding to the other loading paths. Then the K-L transform is applied a second time with the modes selected for each loading path as new snapshots. One could think that the same result would be achieved by applying the K-L transform in one step to all snapshots mixing all loading paths, but this is not the case. Our experience is that the most accurate predictions are obtained with the modes generated by a double application of the K-L transform.

In conclusion, after (re-iterated) application of the Karhunen-Loève transform, M modes have been constructed. These modes are orthogonal to each other, they are incompressible and normalized:

$$\langle \boldsymbol{\mu}^{(k)} : \boldsymbol{\mu}^{(\ell)} \rangle = 0 \quad k \neq \ell, \quad \langle \mu_{eq}^{(k)} \rangle = 1, \quad \mathrm{tr}(\boldsymbol{\mu}^{(k)}) = 0.$$

3.4.2. Local or global modes?

In the early version of the NTFA (Michel and Suquet, 2003), deviced for nonlinear constituents, the modes are defined independently in each individual phase. The restrictions of the snapshots of the viscous strains to each individual phase are stored and processed by the K-L transform. In other words, there are as many sets of modes as phases. The independence of the modes from one phase to the other is essential in deriving the systems of differential equations for the reduced stress $\tau^{(k)}$ whose evolution is governed by the other reduced stresses *from the same phase* (projection of the stress on the modes in a given phase) but not by those of the other phases. In this sense, this earlier approach leads to *local modes* defined independently in the different phases.

In the present study where the phases have a linear behavior, the differential equations for the reduced stresses can be derived without the assumption that the modes are localized in a single phase (see the derivation of eq. (13) where the linearity of the relation between the viscous strain and the stress plays a crucial role). Therefore the modes can alternatively be defined over the whole volume element V. These modes will be called *global modes*. Note that the above mentioned local modes *are not* simply the restriction to each phase of the global modes.

Both definitions of modes, local or global, have been used in the course of the present study.

1. For the local modes which is the original setting of the NTFA (Michel and Suquet, 2003), we have 7 loading paths, 25 snapshots per paths and 3 phases, hence a total of 525 snapshots. After the first application of the K-L transform and with the threshold value $\alpha = 0.9999$, the K-L transform selects 3 modes for each loading path, hence a total of 21 modes per phase, and 63 modes for the 3 phases altogether. When the K-L transform is run for the second time, phase by phase, but combining the 21 modes obtained for the different loading paths, 18 new modes are generated for each individual phase, hence a total of 54 modes for the 3 phases.
2. The same procedure is followed for the global modes approach. To achieve the same required accuracy α, 3 modes are required for each loading path, hence a total of 21 modes. Then, when the K-L transform is run again on these 21 modes, 18 modes are generated.

The two approaches are illustrated in Figure 3. The first modes extracted in each phase by the application of the K-L transform (iterated) are shown in subfigures (a), (b) and (c). The last subfigure (d) shows the first global mode over the whole volume element for the same loading path. As can be seen the local modes are not just the restriction to the phases of the global mode.

The approach by global modes requires less internal variables at the macroscopic scale (18 internal variables instead of 54) and it is certainly more attractive from the point of view of the cost of the structural calculations performed with the effective constitutive relations (17). However, before concluding in favor of the global approach, it is worth comparing the accuracy of both approaches on more complex loading paths, with or without aging of the constituents.

4. Non-aging constituents

To check the accuracy of the two NTFA approaches, with global and local modes respectively, four tests have been performed. In this section, aging of the constituents is not taken into account.

Test 1. Radial monotonic loading along a stress direction which has not been used for the identification of the modes, involving tension and torsion along the first axis:

$$\boldsymbol{\Sigma}^0 = \frac{1}{\sqrt{2}} \left(\boldsymbol{e_1} \otimes \boldsymbol{e_1} + \boldsymbol{e_1} \otimes_s \boldsymbol{e_2} + \boldsymbol{e_1} \otimes_s \boldsymbol{e_3} \right). \tag{20}$$

The volume element is loaded at constant strain-rate $\dot{\overline{\boldsymbol{\varepsilon}}} : \boldsymbol{\Sigma}^0 = (1/\sqrt{2}) 10^{-2} s^{-1}$ for 10 s.

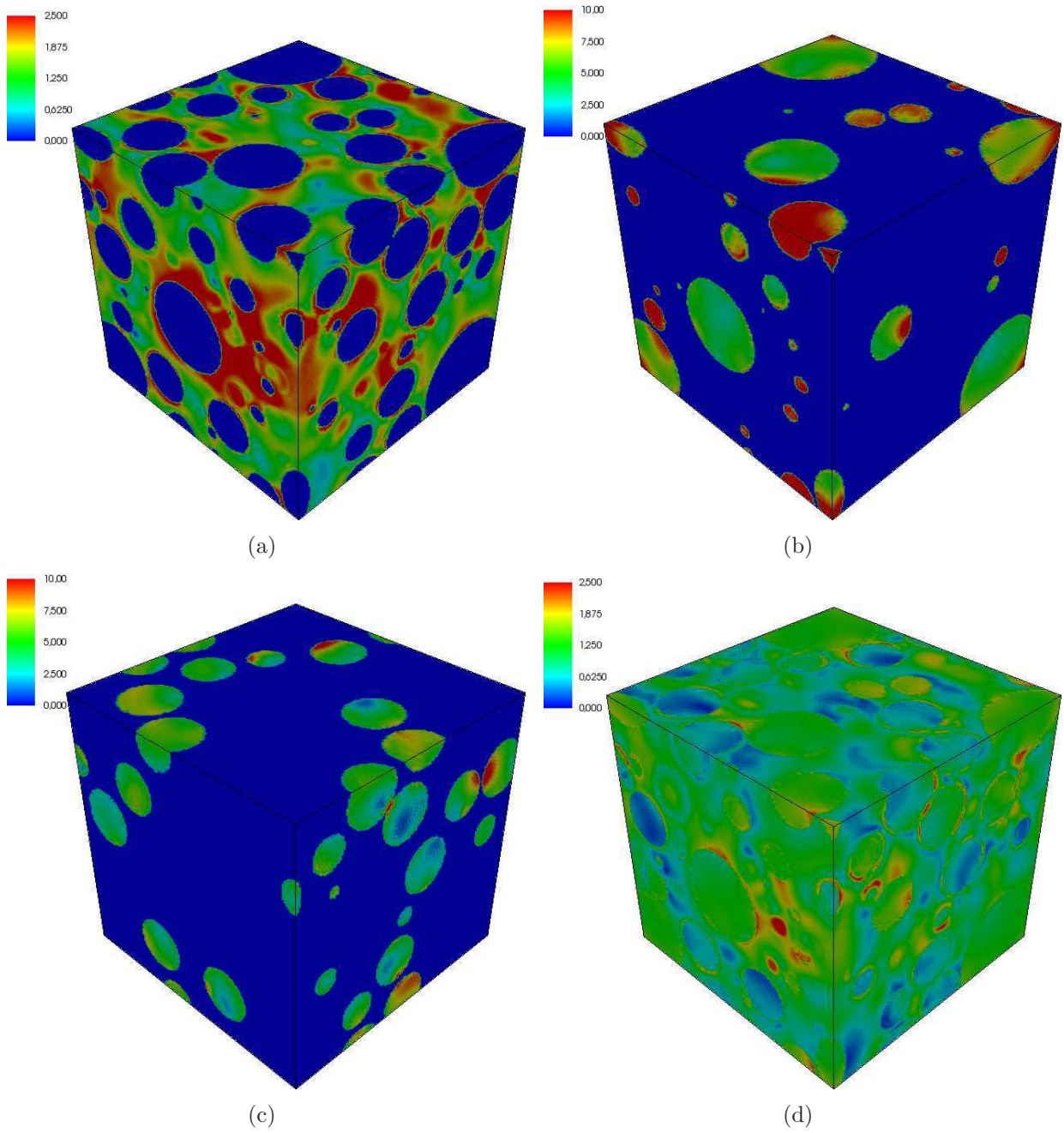

Figure 3: Snapshot of $\mu_{eq}^{(1)}$. (a): First local mode in phase 1 (matrix). (b): First local mode in phase 2 (Pu clusters). (c): First local mode in phase 3 (U clusters). (d): First global mode.

Test 2. A creep test in uniaxial tension in direction 3:

$$\boldsymbol{\Sigma}^0 = \boldsymbol{e}_3 \otimes \boldsymbol{e}_3.$$

First a linear ramp is applied in 0.1 s from $\overline{\sigma}_{33} = 0$ to $\overline{\sigma}_{33} = 100$ MPa. Then $\overline{\sigma}_{33}$ is kept fixed (= 100 MPa).

Test 3. A relaxation test under uniaxial tension ($\overline{\sigma}_{ij} = 0$, except $\overline{\sigma}_{33}$). The overall strain in direction 3 is increased in 0.1 s from 0 to $\overline{\varepsilon}_{33} = 0.02$ and kept constant.

Test 4. A non radial test involving a rotation of principal axes of the overall stress. The overall strain is imposed in the form

$$\overline{\boldsymbol{\varepsilon}}(t) = \varepsilon_0 \sin \omega t \left[\boldsymbol{e_1} \otimes \boldsymbol{e_1} - \frac{1}{2}\boldsymbol{e_2} \otimes \boldsymbol{e_2} - \frac{1}{2}\boldsymbol{e_3} \otimes \boldsymbol{e_3} \right] + \varepsilon_0 (1 - cos(\omega t)) \left[\boldsymbol{e_1} \otimes_s \boldsymbol{e_2} + \boldsymbol{e_1} \otimes_s \boldsymbol{e_3} \right], \tag{21}$$

with $\varepsilon_0 = 0.1$, $\omega = \frac{\pi}{2}$. Swelling is not activated. The response of the volume element is investigated for the first 5 cycles (20 s).

For all 4 tests, the predictions of the two NTFA approaches (with global or local modes) are compared with reference results obtained by full-field simulations using the material data in Table 1. For completeness, the predictions of the TFA method (where the viscous strain is assumed to be uniform within each individual phase) have also been added for Test 1.

The comparison is carried out for three types of information:

i) the effective response of the composite,

ii) the average response of the phases,

iii) the distribution of the stress field in the phases.

4.1. Effective response

The predictions of the two NTFA approaches, with global and local modes, for the overall response of the composite are compared in Figure 4. In Figure 4(a), the prediction of the TFA is also shown. The following comments can be made:

1. The predictions of the TFA deviate significantly from the full-field simulations.
2. Both NTFA approaches are in excellent agreement with the reference results. In other words, the coarser model (NTFA with global modes with 18 internal variables) is as accurate as the finer one (NTFA with modes per phase with 54 internal variables), at least for predicting the effective response of the composite.
3. It worth noting that although the modes have been generated from a set of snapshots corresponding to monotonic loading along specific directions, the NTFA models are still accurate for the more complex loadings of tests 2, 3, 4.
4. The same conclusion applies with or without swelling in the phases.

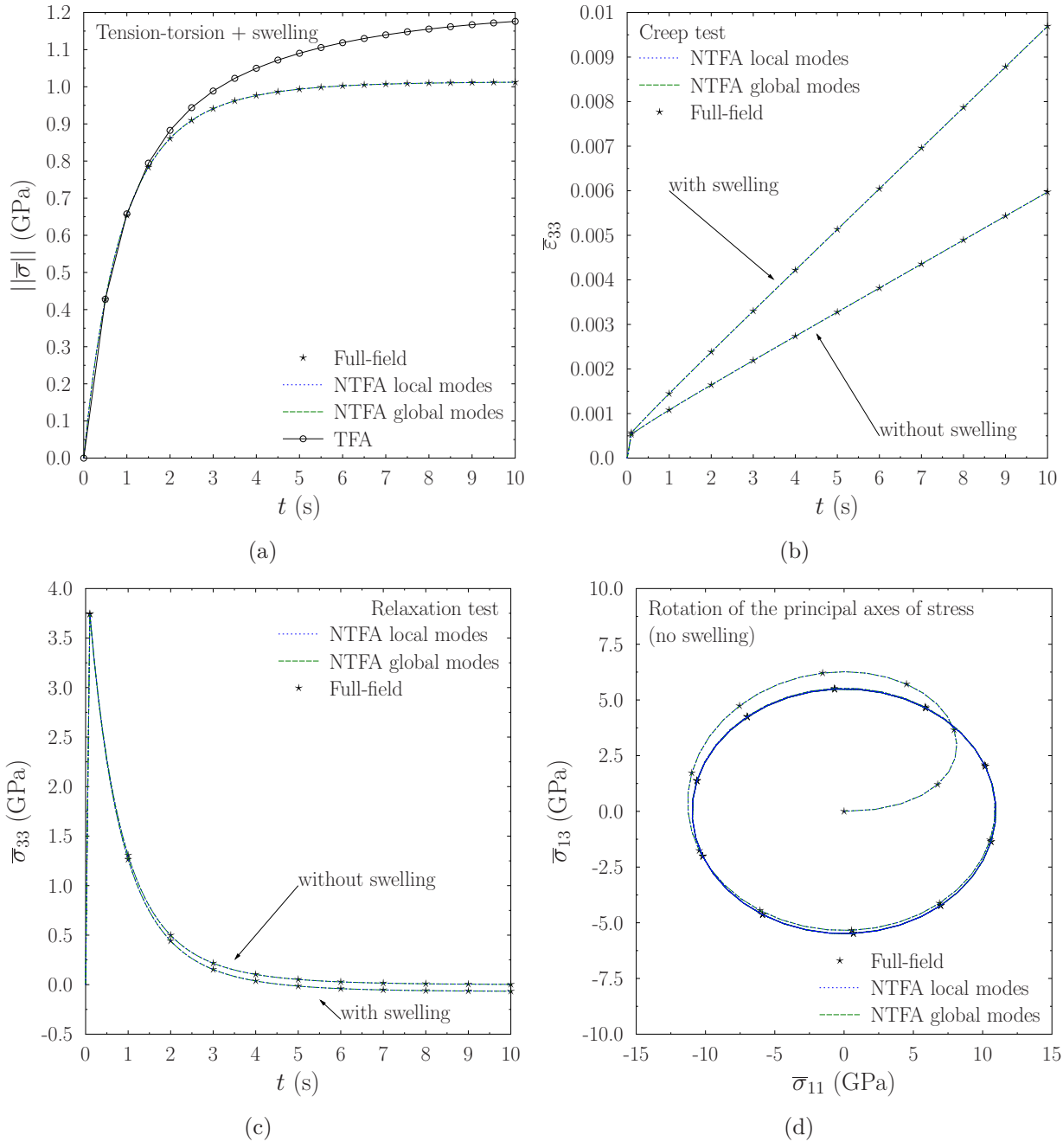

Figure 4: Non-aging constituents - Effective response. Comparison between full-field simulations (symbols) and the two NTFA approaches with global modes (dashed line) and with local modes (dotted line). (a): Test 1. (b) Test 2. (c): Test 3. (d): Test 4.

4.2. Average response of the phases

The average of the stress in the three different phases are compared in Figure 5a, c, d for tests 1, 3, 4 and the average strain in the phases is shown in Figure 5b. The norm of the average stress $\overline{\boldsymbol{\sigma}}^{(r)}$ in each constituent is used for this comparison:

$$\overline{\sigma}_{ij}^{(r)} = \frac{1}{V_r}\int_{V_r} \sigma_{ij}(\boldsymbol{x})\ d\boldsymbol{x}, \quad \left|\left|\overline{\boldsymbol{\sigma}}^{(r)}\right|\right| = \left(\sum_{i,j=1}^{3} \overline{\sigma}_{ij}^{(r)}\overline{\sigma}_{ij}^{(r)}\right)^{1/2}. \tag{22}$$

The predictions of the TFA are clearly unrealistic and will not be investigated further. The agreement of the two NTFA approaches with the reference results is again excellent, both with swelling and without swelling. In test 3 (relaxation), both approaches are able to capture the quick relaxation of stress in the the Pu phase, followed by a progressive reloading of this phase, consequence of swelling and of the relaxation of the two other phases. This illustrates the fact that even though the overall loading is monotonic, the local response in the phases can be quite complex, a complexity that the NTFA captures well.

4.3. Local stress fields

The local stress fields in the phases at the end of test 1 (at t=10 s) and test 4 (at t=20 s) reconstructed by means of the relation (15) are compared in Figures 6, 7 and 8 where the local norm of $\boldsymbol{\sigma}$, defined as

$$||\boldsymbol{\sigma}(\boldsymbol{x})|| = \left(\sum_{i,j=1}^{3} \sigma_{ij}(\boldsymbol{x})\sigma_{ij}(\boldsymbol{x})\right)^{1/2}, \tag{23}$$

is plotted. They can hardly been distinguished. It is only when comparing the probability distribution of the stress fields in the phases that a slight discrepancy can be observed. This is done in Figure 9 for test 1 and Figure 10 for test 4. The NTFA approach with local modes (dotted line) fits well the full-field simulations, whereas a little deviation can be seen with the NTFA approach with global modes. But the discrepancy remains small (compared to the dispersion of the results for different realizations, see Appendix A) and both NTFA approaches can be considered as being in excellent agreement with the reference results.

4.4. Gain in computational time

The CPU times for the different methods (TFA, NTFA with global modes, NTFA with local modes and full-field simulations) have been compared for Test 1. The different CPU times (Intel Core i7-2920XM) are as follows:

- Full-field simulations (discretization in 147^3 voxels): 1231 s.
- TFA (18 internal variables): 0.018s.
- NTFA with local modes (54 internal variables): 0.64s.
- NTFA with global modes (18 internal variables): 0.046 s.

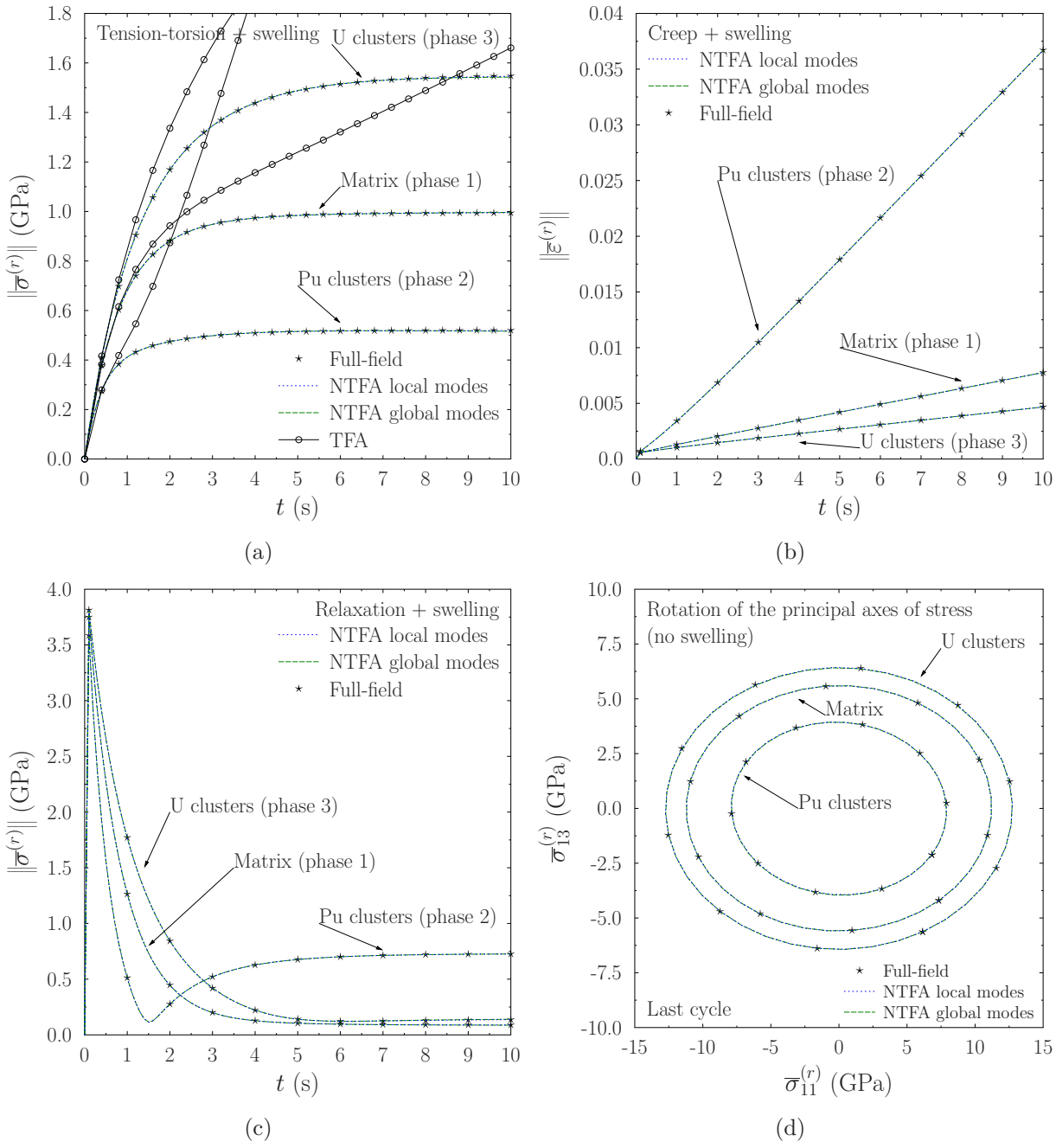

Figure 5: Non-aging constituents -Average response of the phases. Comparison between full-field simulations (symbols), the NTFA approach with global modes (dashed line) and the NTFA approach with local modes (dotted line). (a): Test 1. (b): Test 2. (c): Test 3. (d): Test 4, last cycle.

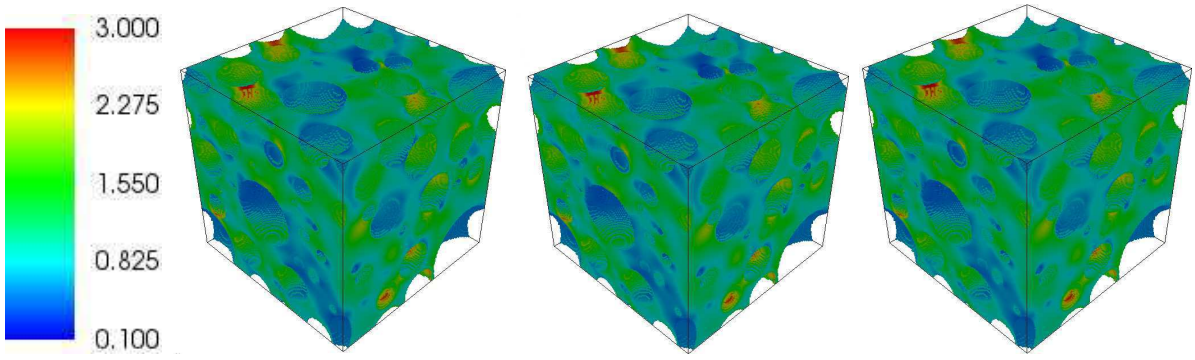

(a) (b) (c)

Figure 6: Non-aging constituents. Norm of the stress field in the matrix (units: GPa). (a): Full-field. (b): NTFA with local modes. (c): NTFA with global modes.

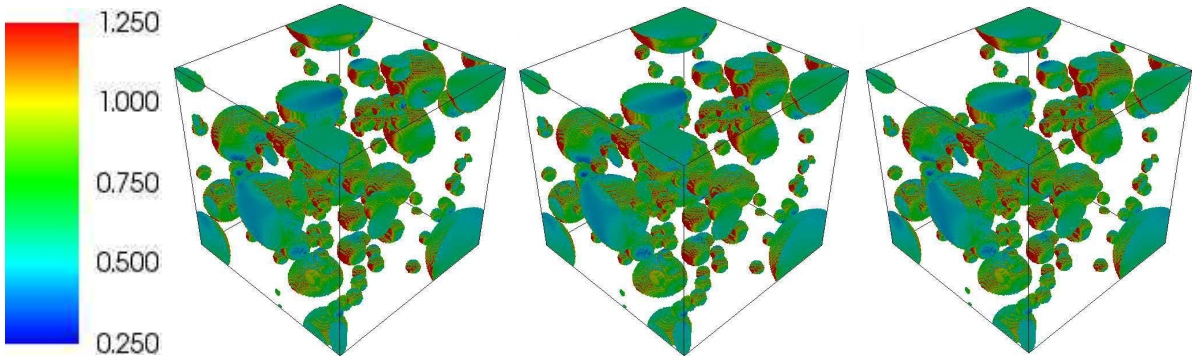

(a) (b) (c)

Figure 7: Non-aging constituents. Norm of the stress field in the Pu clusters (units: GPa). (a): Full-field. (b): NTFA with local modes. (c): NTFA with global modes.

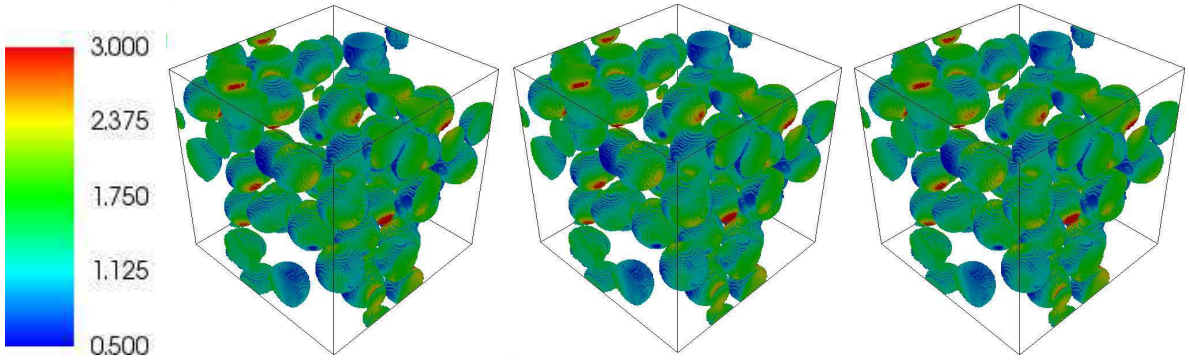

(a) (b) (c)

Figure 8: Non-aging constituents. Norm of the stress field in the U clusters (units: GPa). (a): Full-field. (b): NTFA with local modes. (c): NTFA with global modes.

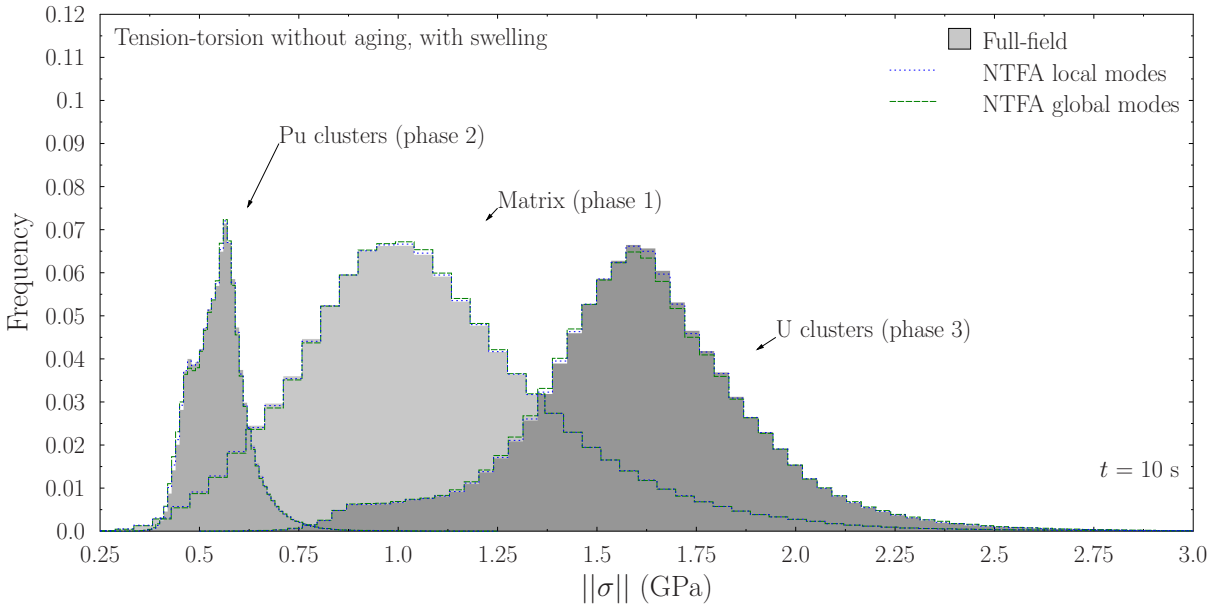

Figure 9: Non-aging constituents. Test 1. Probability distribution of the norm of the stress field in the different phases at $t = 10$ s.

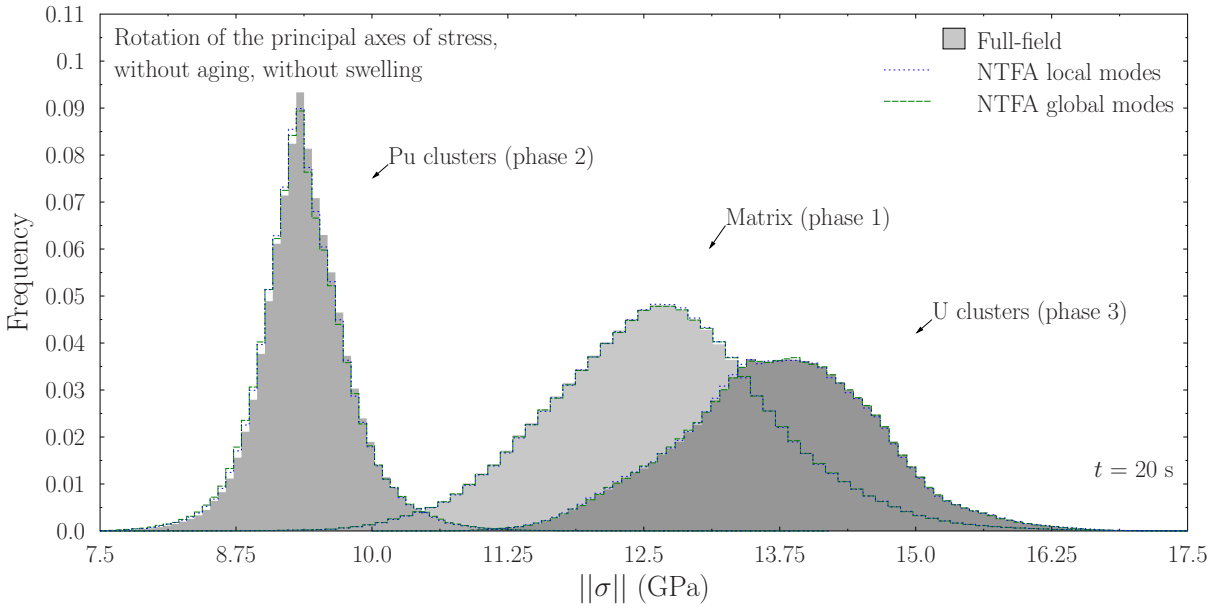

Figure 10: Non-aging constituents - Test 4 - Probability distribution of the norm of the stress field in the different phases at $t = 20s$.

The TFA is the costless method but is, by far, too inaccurate. Its accuracy can be improved by subdividing the phases into several subdomains but then its costs will be much larger than that of the NTFA with less accuracy. The gain in CPU times obtained by using the NTFA with global modes over the full-field simulations is 2×10^4. This is quite significant. Finally the two NTFA methods with local and global modes differ in cost by a factor of 10 approximatively.

4.5. Conclusions

For non-aging constituents the predictions of both NTFA approaches, with modes defined in the whole volume or per phase, with or without swelling in the phases, are in excellent agreement with full-field simulations over a wide variety of loading paths. Given that the NTFA with global modes has less internal variables (18 instead of 54 in the NTFA approach wih local modes), the use of this reduced model seems amply sufficient for macroscopic structural calculations. The objective of the next section is to check the validity of this conclusion for aging constituents.

5. Composites with aging constituents

When the constituents of the composite are subject to aging, care should be used in the choice of the modes on which the decomposition (6) is based. By construction the modes do not depend on time, unlike the material properties of the constituents which, because of aging, vary with time. Therefore it is not clear which material data should be used in the tests from which the modes are constructed. A first possibility is to construct the modes as in section 4 with the *initial* material properties of the phases and *to keep them unchanged through the whole evolution process* of the material. The question which arises naturally is whether these modes, which are relevant in the initial stage of the deformation, contain sufficient information on the deformation of the microstructure throughout the whole loading history. Another possibility would be to use the material data at the end of the aging history or the actual aging properties, whenever they are known, to generate the modes. A last possibility is to mix the two sets of modes obtained with the initial and final material properties. The aim of this section is to investigate these different possibilities.

5.1. Aging constituents

The level of aging of the constituents depends on the history of irradiation to which the fuel is subjected. Since irradiation is a known function of time, specifying an aging history is equivalent to specifying a time dependence of the material properties of the constituents. Aging affects mostly the viscosity $G_{\mathrm{v}}^{(r)}$ of the individual constituents (Scdap Relap5, 1997), or equivalently their fluidity defined as $1/G_{\mathrm{v}}^{(r)}$, whereas the other material properties (elasticity, swelling rate) can be considered as time independent.

Since aging softens the matrix (phase 1), the matrix fluidity increases with irradiation, corresponding to an acceleration of the creeping-rate. The increase in matrix fluidity with irradiation is a consequence of the increase in content of the plutonium (239 and 241) by neutron capture from uranium (238). To make things simple the variations of the matrix fluidity with respect to time on an interval of study $[0, T]$ are assumed to be bilinear, with a first linear ramp from 0 to a transition time t_1 and a second ramp from t_1 to the final

time T (see Appendix C). The two intervals $[0, t_1]$ and $[t_1, T]$ correspond for instance to two different regimes of irradiation. The first interval corresponds to the case where uranium (238) and plutonium (239 and 241) contents are hardly consumed. This regime of irradiation is representative of low power pressure water reactor (PWR) conditions. The second interval corresponds to the case where the plutonium (239 and 241) and uranium (238) contents are consumed. This regime of irradiation is representative of PWR nominal conditions. The specific expression of $G_{\mathrm{v}}^{(1)}(t)$ corresponding to the plots of Figure 11 is given in Appendix C. It was obtained by the neutron model of the nuclear fuel code Cyrano3 (Baron et al., 2008).

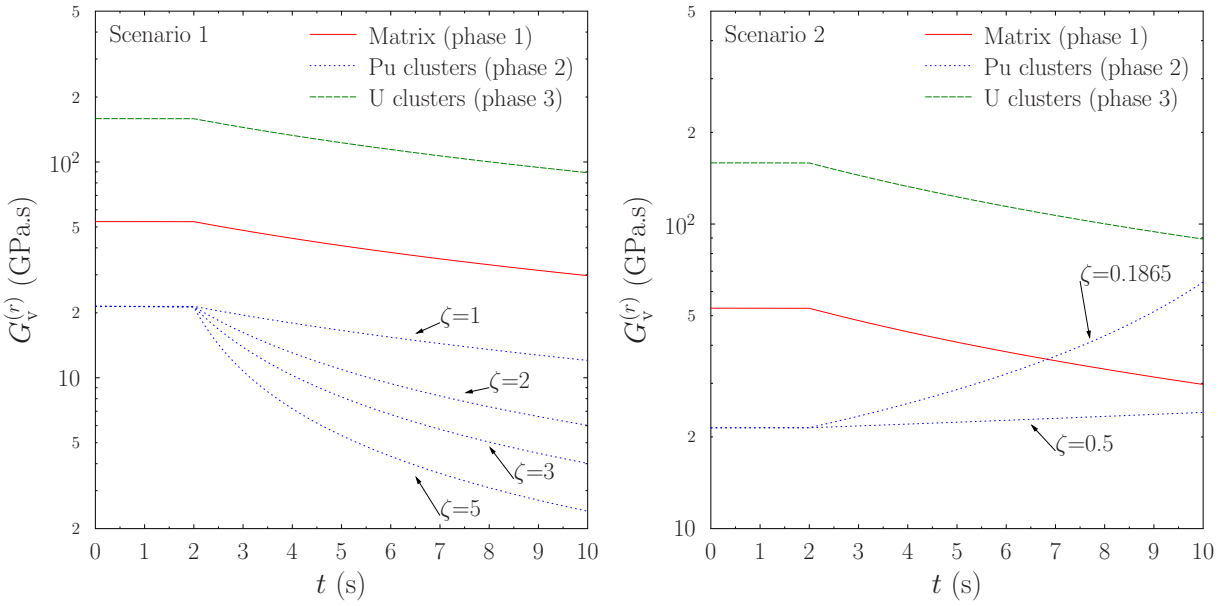

Figure 11: Aging constituents - Different scenarii for the evolution of $G_{\mathrm{v}}^{(r)}(t)$ with time for the three phases.

The U clusters follow the same trend as the matrix but creep 3 times slower since the plutonium content is lower. Therefore the viscosities of phase 1 and phase 3 are linked through

$$G_{\mathrm{v}}^{(3)}(t) = 3G_{\mathrm{v}}^{(1)}(t),$$

and the evolution in time of the viscosity in the matrix and in the U clusters are parallel (Figure 11).

As for the Pu phase, its viscosity is initially the lowest of the three phases (Table 1), which corresponds to creep eigenstrains in the Pu phase being 2.5 time larger than in the matrix. Two scenarii for the time-dependence of the creeping properties of the Pu phase have been investigated corresponding either to softening or hardening of this phase relative to the matrix. These scenarii differ by the value of the parameter ζ which measures the variation of the

viscosity contrast between the Pu phase and the matrix :

$$\zeta = \left(\frac{G_{\mathsf{v}}^{(2)}(0)}{G_{\mathsf{v}}^{(1)}(0)}\right) / \left(\frac{G_{\mathsf{v}}^{(2)}(T)}{G_{\mathsf{v}}^{(1)}(T)}\right) \tag{24}$$

$\frac{G_{\mathsf{v}}^{(2)}(0)}{G_{\mathsf{v}}^{(1)}(0)}$ is the initial contrast between the Pu and the matrix, $\frac{G_{\mathsf{v}}^{(2)}(T)}{G_{\mathsf{v}}^{(1)}(T)}$ is the final contrast and ζ is the ratio between the initial and the final contrast. According to Table 1, the initial contrast is around 0.4.

1. The first scenario (Figure 11 left) corresponds to a softening of the Pu phase with respect to the matrix
$$\frac{G_{\mathsf{v}}^{(2)}(T)}{G_{\mathsf{v}}^{(1)}(T)} \leq \frac{G_{\mathsf{v}}^{(2)}(0)}{G_{\mathsf{v}}^{(1)}(0)}, \quad i.e. \quad \zeta \geq 1.$$
The viscosity of phase 2 (Pu) is a decreasing function of time, as in the other phases. The contrast between the Pu phase and the matrix is strengthened by aging. The deformation patterns should not change dramatically, the deformation being concentrated in the Pu inclusions and in zones linking them. The effect of the strengthening of the contrast should only be to increase the strain concentration in these zones.
2. In the second scenario (Figure 11 right) the Pu phase hardens with respect to the matrix,
$$\frac{G_{\mathsf{v}}^{(2)}(T)}{G_{\mathsf{v}}^{(1)}(T)} \geq \frac{G_{\mathsf{v}}^{(2)}(0)}{G_{\mathsf{v}}^{(1)}(0)}, \quad i.e. \quad \zeta \leq 1.$$
When $\zeta = 1$ the contrast between the phases does not change and the corresponding plots of the viscosities for the three phases are parallel (Figure 11 left). When $\zeta \leq \frac{G_{\mathsf{v}}^{(2)}(0)}{G_{\mathsf{v}}^{(1)}(0)} \simeq 0.57$ the viscosity of the Pu phase is an increasing function of time. And when $\zeta \leq \frac{G_{\mathsf{v}}^{(2)}(0)}{G_{\mathsf{v}}^{(1)}(0)} \simeq 0.4$ the contrast between the two phases is reversed: the Pu phase which was initially the softer phase becomes stiffer than the matrix (Figure 11 right). This inversion of the contrast between the viscosity of the matrix and of the Pu clusters corresponds to an inversion of the magnitude of the creep strains in the phases and to a dramatic change in the deformation patterns. The question worth of investigation is how the NTFA can handle such an inversion with the same modes throughout the process.

It should be noted that the actual MOX behavior under irradiation corresponds to $\frac{G_{\mathsf{v}}^{(2)}(0)}{G_{\mathsf{v}}^{(1)}(0)} \simeq 0.4 \leq \zeta \leq \frac{G_{\mathsf{v}}^{(2)}(0)}{G_{\mathsf{v}}^{(1)}(0)} \simeq 0.57$. The other cases are parametric studies considered for completeness.

The ability of the NTFA approaches to capture accurately the overall response of the composite as well as the local fields in the phases when the viscosities are time dependent has been investigated for the two scenarii. In both cases, the loading is a radial path along the stress direction (20) combining tension and torsion, the phase viscosities depend on time and swelling is taken into account.

5.2. Scenario 1. Softening of the Pu clusters with respect to the matrix: $\zeta \geq 1$.

In a first attempt the *initial modes* constructed in section 4, corresponding to the initial material data, were used in the two NTFA approaches (with global and local modes). Four different values of ζ ($\zeta = 1, 2, 3, 5$) were investigated. The effective response of the composite is shown in Figure 12(a). For all values of ζ the predictions of both NTFA approaches are in good agreement with the full field simulations. When one turns to the average response of the

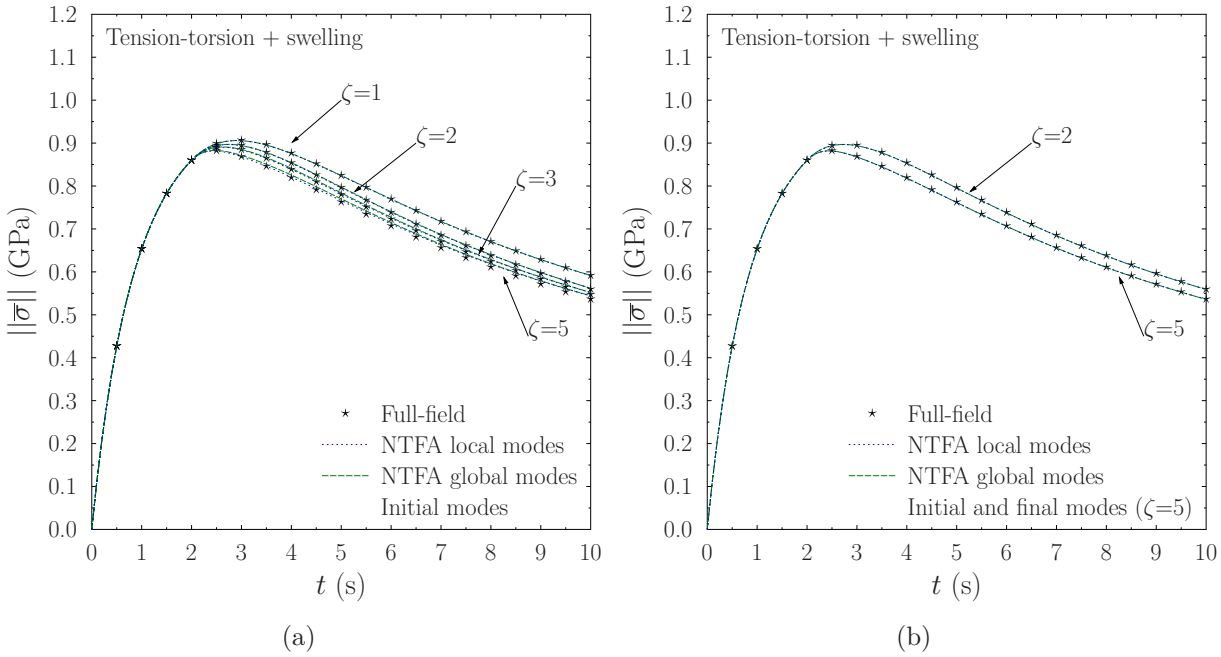

Figure 12: Aging constituents. Combined tension, torsion and swelling. Scenario 1: increased contrast between the Pu clusters and the matrix. Effective response. Comparison of the predictions of the NTFA with global modes (dashed line) and local modes (dotted line) with full-field simulations (symbols). (a) Initial modes. (b) Initial and final modes. The final modes are computed with the material data corresponding to $\zeta = 5$.

phases the predictions for the average stress in the phases deviate from the reference results as ζ increases and this deviation increases with time (Figure 13). The softer the Pu phase in its final state, the larger the deviation. This deviation on the averaged quantities reflects an even larger deviation on the local fields.

This has motivated the introduction of a second set of modes. First the *final modes* corresponding to the *final* material data at $t = T$ and for $\zeta = 5$ are generated. For the same value of α 18 modes are required in the NTFA model with global modes and 54 modes in the approach with local modes. Then the two sets of modes, initial and final, are merged and become a new set of snapshots from which new orthogonal modes are generated by means of the K-L transform. The new set of modes has 36 and 108 modes respectively for the two approaches (for the same content of information $\alpha = 1 - 10^{-4}$). The K-L transform does not reduce the number of modes and this can be attributed to significant differences between the initial and the final modes. The two NTFA approaches are implemented with the new sets of modes and

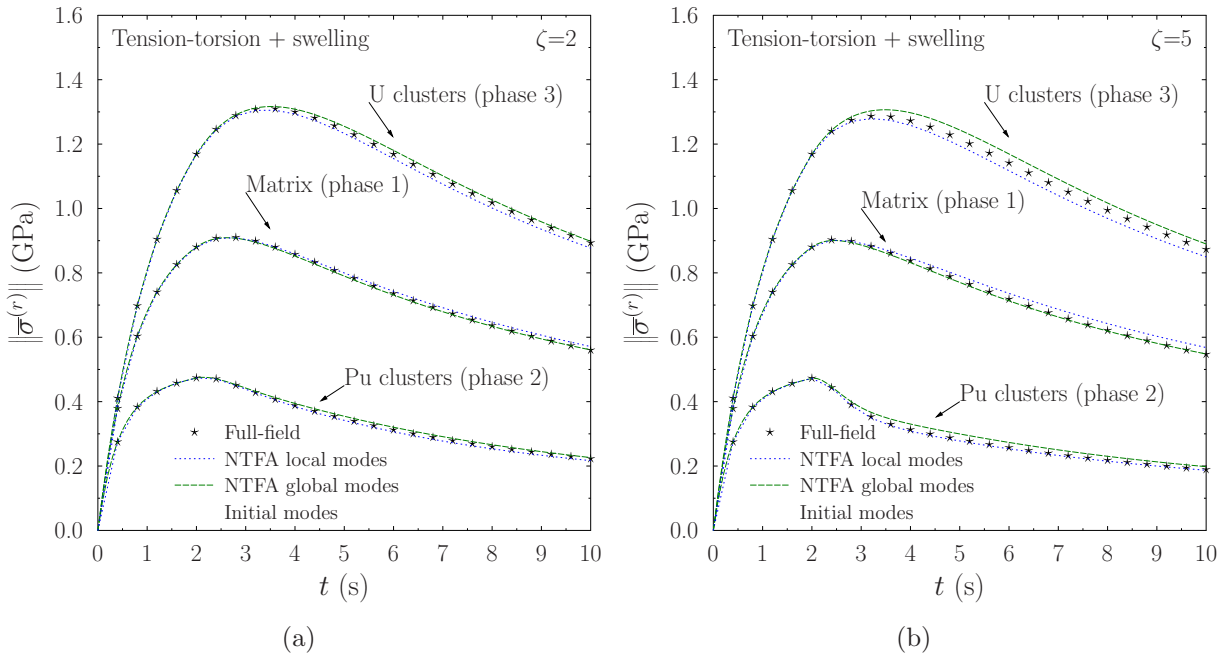

Figure 13: Aging constituents. Combined tension, torsion and swelling. Scenario 1: increased contrast between the Pu clusters and the matrix. Average stress in the individual phases. Comparison between full-field simulations (symbols) and the two NTFA approaches, with global modes (dashed line) and with local modes (dotted line). Modes generated with the initial material data. (a): $\zeta = 2$. (b): $\zeta = 5$.

the predictions for $\zeta = 2$ and $\zeta = 5$ are shown in Figure 14. Even though the final modes have been computed only for $\zeta = 5$, the agreement is excellent for $\zeta = 2$ and $\zeta = 5$, both for the effective response (Figure 12(b)) and for the average stress in the phases (Figure 14). If we now

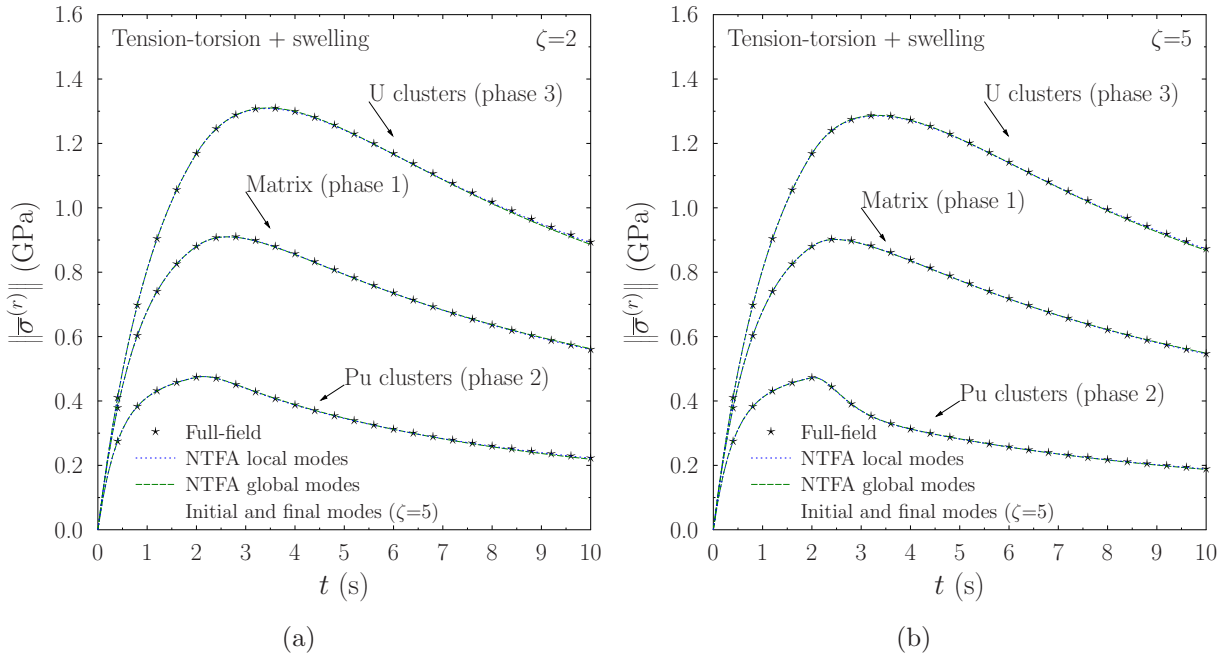

Figure 14: Aging constituents. Combined tension, torsion and swelling. Scenario 1: increased contrast between the Pu clusters and the matrix. Average stress in the individual phases. Combination of initial and final modes (generated with the initial material data and with the final material data with $\zeta = 5$)). Comparison between full-field simulations (symbols) and the two NTFA approaches, with global modes (dashed line) and with local modes (dotted line). (a): $\zeta = 2$. (b): $\zeta = 5$.

turn to more local informations, *i.e.* to the distribution of the stress field in the phases shown in Figure 15, it is observed that the NTFA model with global modes is slightly less accurate than the NTFA approach with local modes, essentially in the U and Pu phases. However the difference remains small and given the reduction in cost provided by the model with global modes, it can be used with a good accuracy.

To conclude this discussion, when aging makes the Pu phase even softer than in its initial condition, the NTFA with the initial global modes can be used to capture accurately the effective response of the composite. However in order for the NTFA to deliver an accurate local response of the composite, use of the NTFA with both the initial and final global modes is recommended. The resulting effective constitutive relations involve 36 internal variables. This number is significant but this is the price to pay to capture accurately both to the effective response and the local fields in the composite throughout its entire time history.

5.3. Scenario 2. Stiffening of the Pu clusters with respect to the matrix

We now turn to the most difficult situation, namely the case where the contrast between the Pu and the matrix switches from the initial state where the Pu inclusions are softer than the

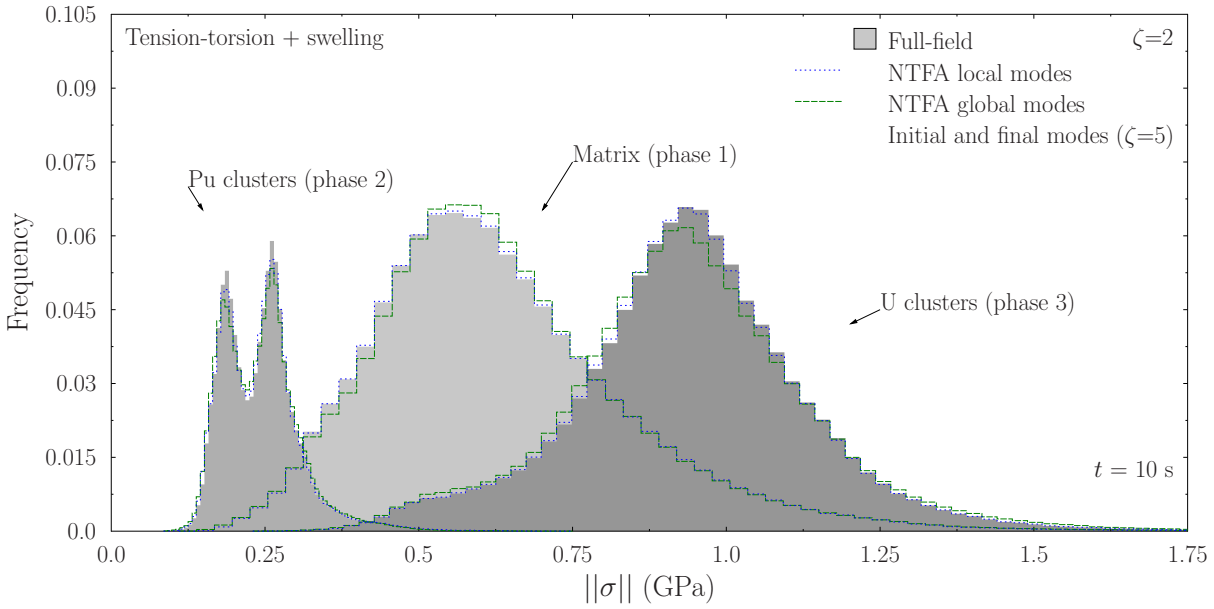

(a)

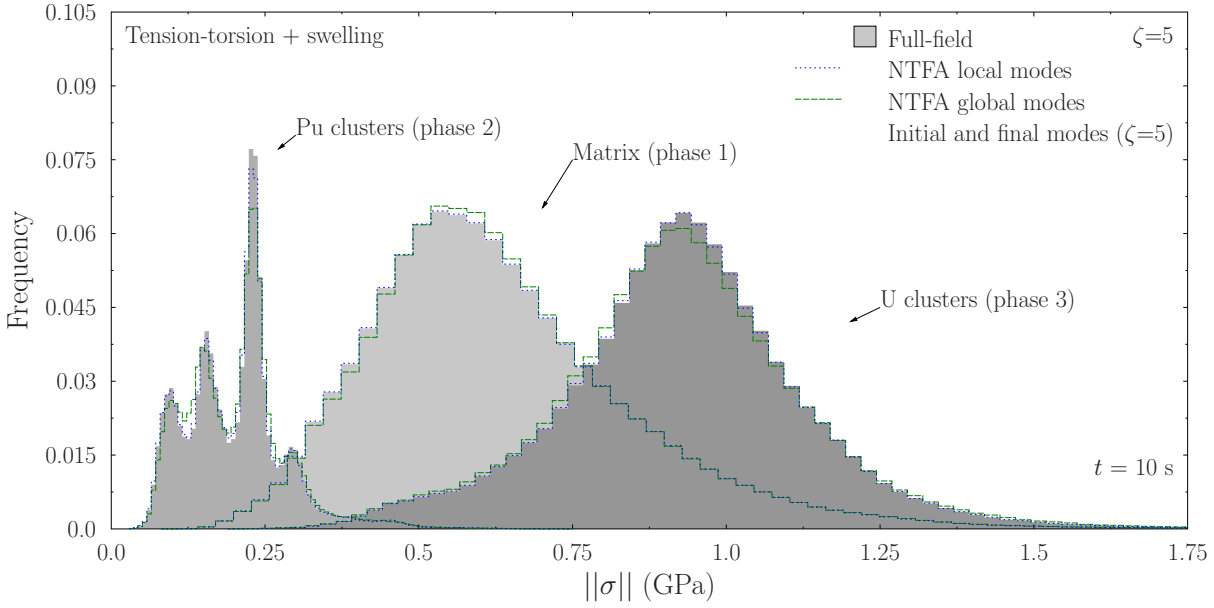

(b)

Figure 15: Aging constituents. Combined tension, torsion and swelling. Scenario 1: increased contrast between the Pu clusters and the matrix. Combination of initial and final modes (generated with the initial material data and with the final material data with $\zeta = 5$). Comparison between full-field simulations (full bars) and the predictions of the NTFA with global modes (dashed line) and local modes (dotted line). (a) $\zeta = 2$. (b) $\zeta = 5$.

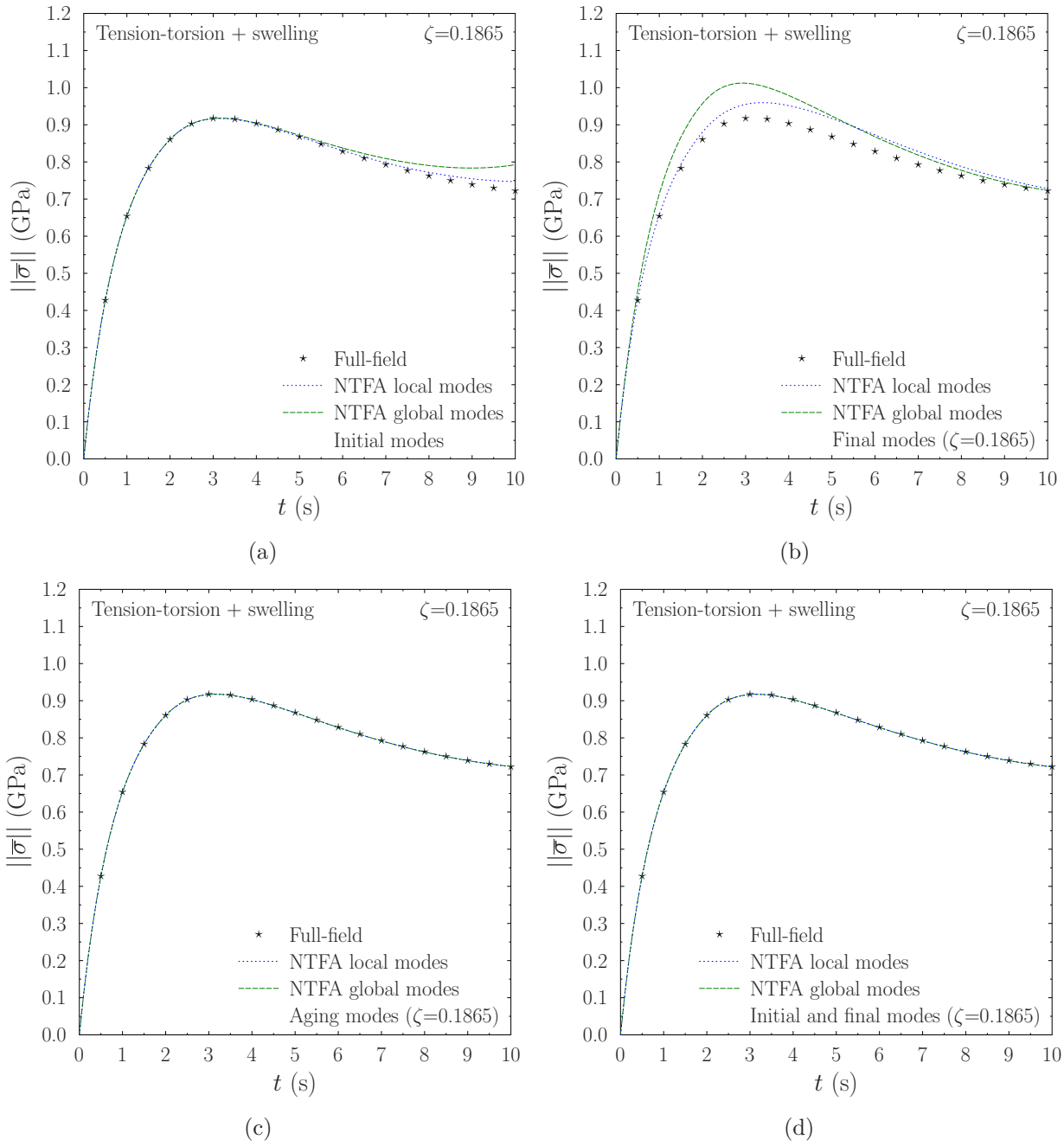

Figure 16: Aging constituents. Combined tension, torsion and swelling. Scenario 2: hardening of the Pu clusters with respect to the matrix with inversion of the contrast ($\zeta = 0.1865$). Effective response of the composite. Comparison between full-field simulations (symbols) and the two NTFA approaches with global modes (dashed line) and local modes (dotted line). (a): with initial modes. (b): with final modes. (c): Modes generated from snapshots obtained with the actual, aging, material data. (d): Combination of the initial and final modes.

matrix (higher fluidity) to the final state where they are stiffer (higher viscosity). This situation corresponds to $\zeta \leq 0.4$. In the specific example under consideration here ζ was chosen equal to 0.1865.

To account for the expected change in the deformation patterns four different set of modes were generated and the predictions of the NTFA approaches for these four sets of modes are compared in Figure 16 with full-field simulations.

a) The first set of modes corresponds to the modes identified in section 4, constructed from snapshots obtained with the *initial* material data given in Table 1. The constitutive relations for the two NTFA approaches involve respectively 18 internal variables (global modes) and 54 internal variables (local modes). It is first observed in Figure 16a that the predictions of both NTFA approaches deviate from the full-field results beyond $t \simeq 7$s, which corresponds to the inversion of the contrast between the matrix and the Pu clusters. Therefore the initial modes give a satisfactory answer before this inversion but not beyond it. A second observation is that the deviation of the NTFA approach with local modes remains smaller than that of the NTFA with global modes. Therefore the NTFA with local modes is preferable when only the initial material data are available.

b) The second set of modes has been generated using the *final* material data (the viscosities of the phases are taken as in Figure 11 at $t = 10$ s). Again, the constitutive relations for the two NTFA approaches involve respectively 18 internal variables (global modes) and 54 internal variables (local modes). Not surprizingly, the predictions of the NTFA approaches at the beginning of the test are not in good agreement with the reference results, as can be seen in Figure 16(b) whereas they come closer to them at the end of the test. The approach with global modes deviates more significantly from the reference than the approach with local modes.

At this stage, it can be concluded that the modes computed with only the initial material data or the final ones do not lead to an accurate description of the effective response over the whole interval of study. The inversion of the contrast between the viscosities leads to a deep change in the deformation patterns. This change is illustrated in Figure 17 where snapshots of the viscous strain at $t = 10$ s computed with the initial material data and with the final material data are shown. When the initial viscosities are used, the viscosity of the Pu clusters being less than the viscosity of the matrix, the viscous strains tend to concentrate in the Pu clusters or to go through them. Conversely, when the final material data are used, the viscosity in the Pu clusters being larger than in the matrix, the strain tends to avoid the Pu clusters and to concentrate in the matrix. A good set of modes must be rich enough to accommodate this transition in the deformation patterns. This is clearly not the case if one chooses either the initial modes or the final ones. In order to complete the missing information in the choices a) and b), two other directions have been explored.

c) A third set of modes was generated using the actual time-dependent viscosities of Figure 11. More modes are necessary to achieve the required accuracy $\alpha = 1 - 10^{-4}$ and the NTFA approaches involve respectively 24 internal variables (global modes) and 72 internal

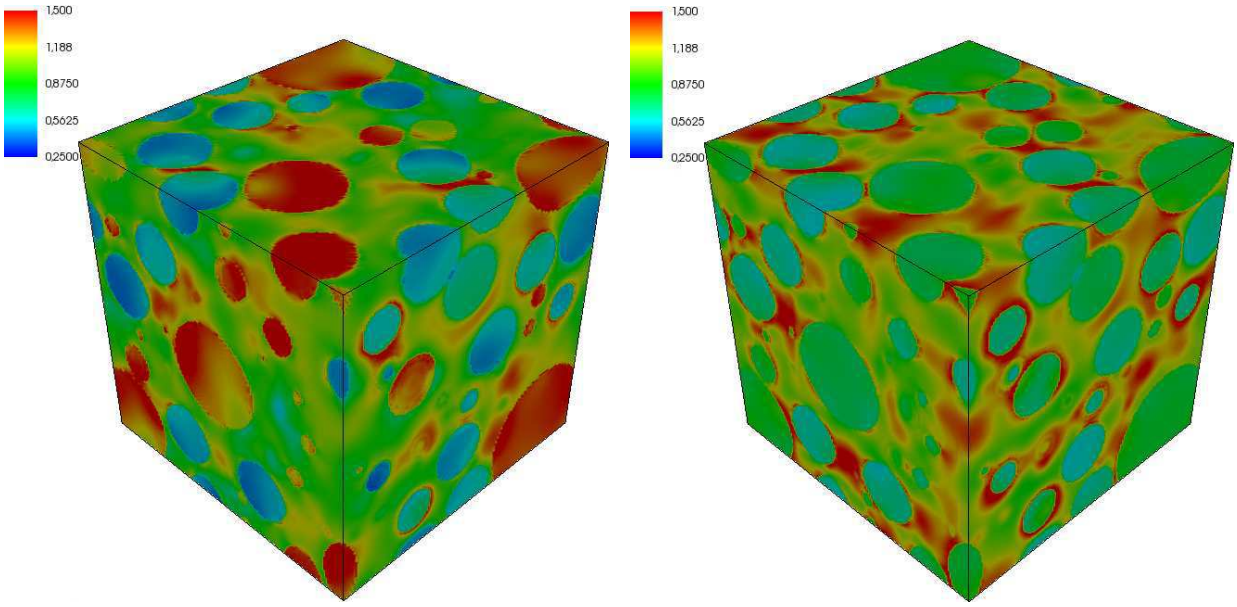

(a) (b)

Figure 17: Aging constituents. Combined tension, torsion and swelling. Scenario 2: hardening of the Pu clusters with respect to the matrix with inversion of the contrast ($\zeta = 0.1865$). Snapshots at $t = 10$ s of $\varepsilon_{\mathsf{v}}^{eq}/\langle\varepsilon_{\mathsf{v}}^{eq}\rangle$ where the field of the equivalent viscous strain $\varepsilon_{\mathsf{v}}^{eq}$ is normalized by its average $\langle\varepsilon_{\mathsf{v}}^{eq}\rangle$. In both snapshots $\langle\varepsilon_{\mathsf{v}}^{eq}\rangle \simeq 0.1$. (a) : Full-field simulation with the initial material data. (b) Full-field simulation with the final material data.

variables (local modes). The agreement of both approaches with full-field simulations is now excellent (Figure 16(c)). The major down side of this way of generating the modes is that the whole time history of the viscosities of the phases is required, whereas in practice one has often access to the initial and final states of the fuel, but not to its intermediate states (which, in addition, may vary with the loading history). This has motivated the investigation of a fourth procedure.

d) Finally the last predictions are obtained by considering *both* set of modes, initial and final, as snapshots, and applying the K-L transform to generate a new set of orthogonal modes. This choice is consistent with the above remark that often only the initial and final state of the material are known. Again the agreement with full field simulations is excellent (Figure 16(d)). However, doubling the number of modes has a cost which is a doubling of the number of internal variables in the constitutive relations: 36 for the global modes, 108 for the local modes. On the other hand, by combining both sets of modes (initial and final) the model is more general and can be expected to cover various loading histories between the initial and the final states of the material.

In conclusion, when the contrast between the viscosities in the matrix and the Pu clusters is reversed, it is not sufficient to use a single set of modes generated with only the initial or the final material data. The best modes are obtained by using the actual aging material data (procedure c). If the history of these material data is not known, the modes obtained with the initial and final material data can be used to generate a new set of modes (procedure d). The predictions for the overall response of the composite of the NTFA method with the modes generated by procedures a and b are not satisfactory for this case with contrast inversion. They will not be discussed any further. On the other hand, the predictions for the overall response of the composite of the NTFA method with the modes generated by procedures c and d (with either local modes or global modes) are excellent. It remains to check that they remain accurate for the field averages and for the field distribution in the phases.

The average stress in the phases are shown in Figure 18. As can be seen the agreement is excellent for both procedures. As for the field distribution, Figure 19 confirms that when the modes are chosen according to procedures c or d the predictions of the NTFA are in good agreement with the full field simulations. Again the NTFA model with global modes is less accurate than the model with local modes. However the accuracy of the NTFA model with global modes is still very satisfactory and, given that this model requires less internal variables (36 for procedure d and 24 for procedure c), it is probably the best choice if the history of the material data is available. The procedure d should be preferred when the time history of the material data is not known.

5.4. Concluding remarks on aging constituents

Two scenarii have been considered in this section for the evolution of the contrast in viscosity between the Pu phase and the matrix. Concerning the choice of the modes, the following observations have been made, depending on the level of information which is expected.

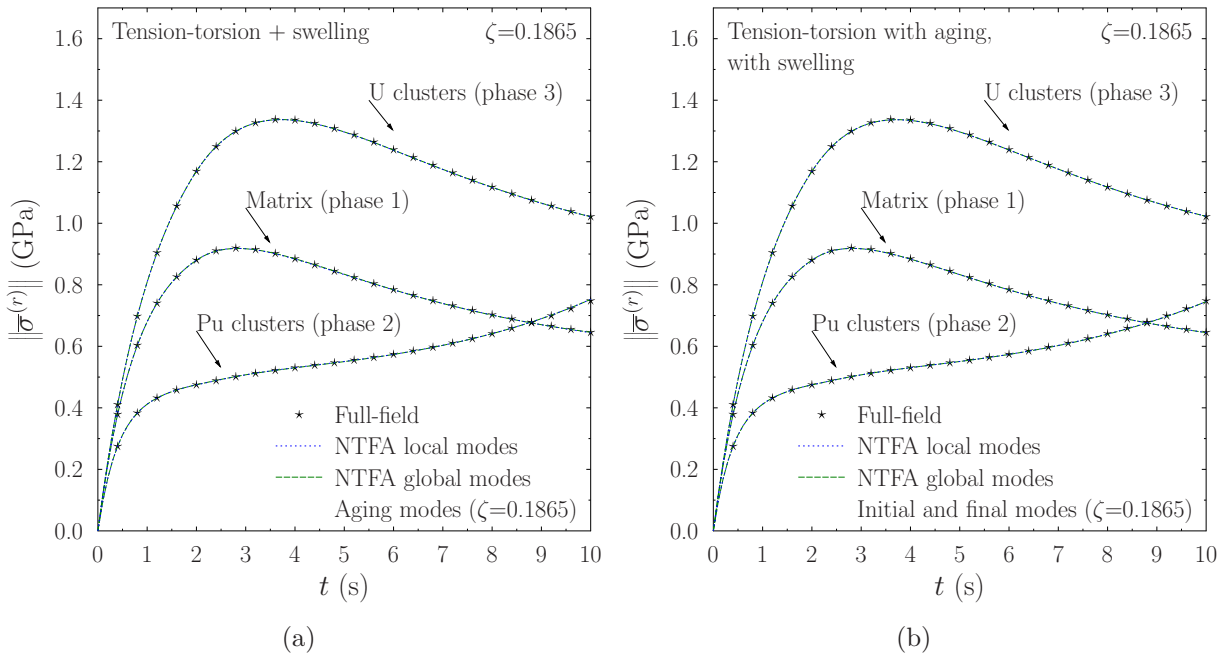

Figure 18: Aging constituents. Combined tension, torsion and swelling. Scenario 2: hardening of the Pu clusters with respect to the matrix with inversion of the contrast ($\zeta = 0.1865$). Average stress in the phases. Comparison between the predictions of the NTFA with global modes (dashed line) and local modes (dotted line) and full-field simulations (symbols). (a): Modes generated with the actual aging material data. (b): Combination of the initial and final modes.

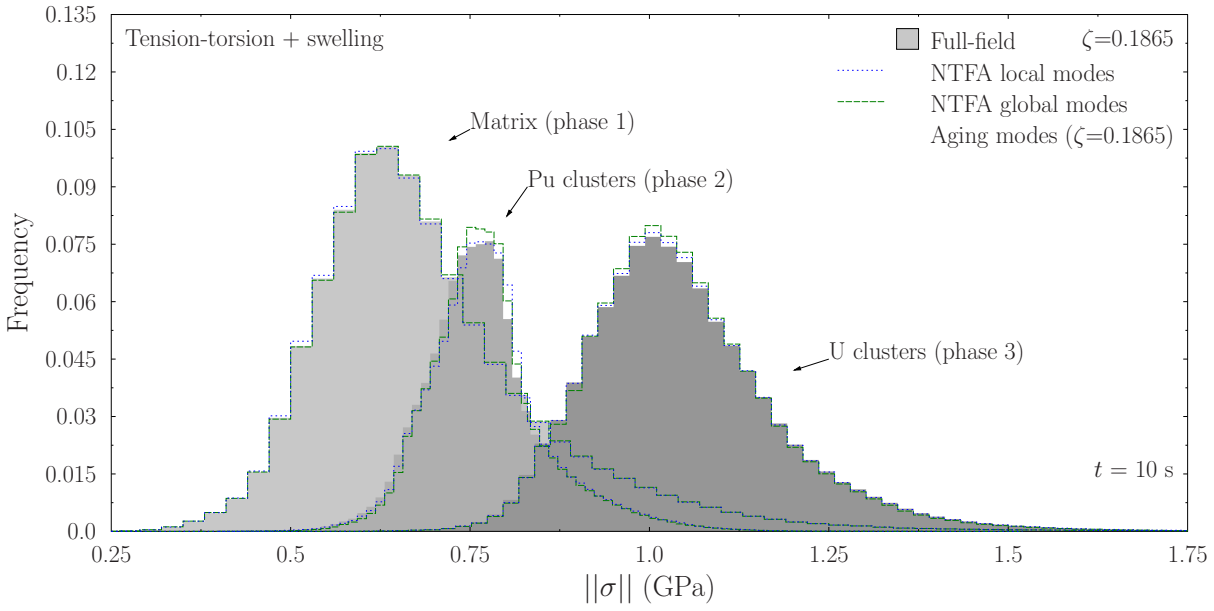

(a)

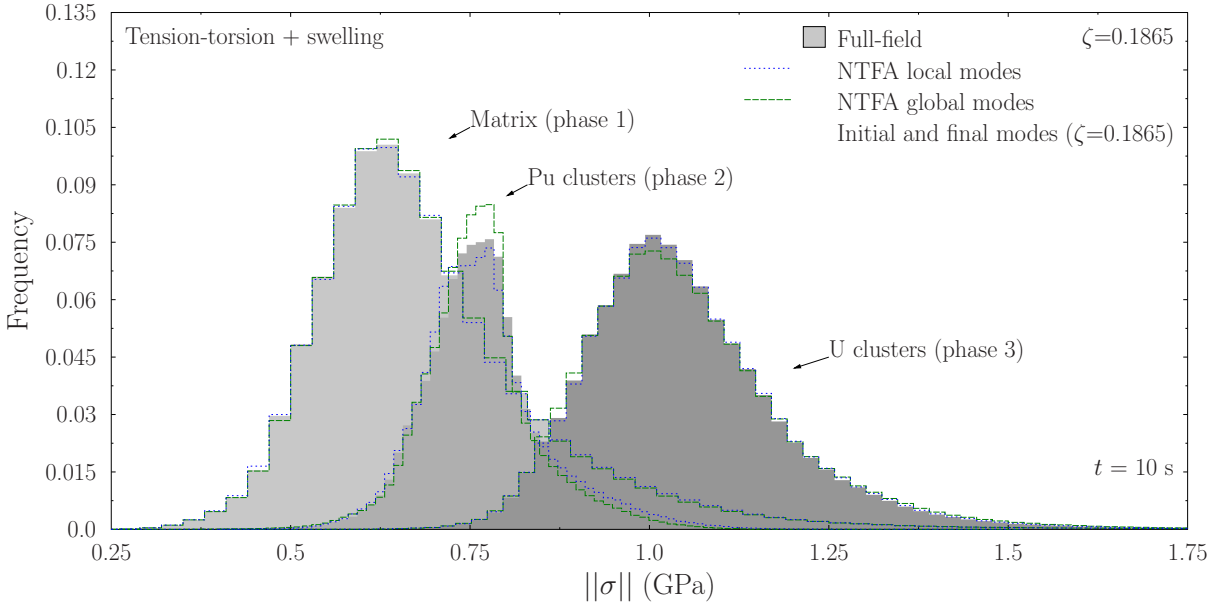

(b)

Figure 19: Aging constituents. Combined tension, torsion and swelling. Scenario 2: hardening of the Pu clusters with respect to the matrix with inversion of the contrast ($\zeta = 0.1865$). Distribution of the stress in the phases. Comparison between the predictions of the NTFA with global modes (dashed line) and local modes (dotted line) and full-field simulations (full bars). (a): Modes generated with the actual aging material data. (b): Combination of the initial and final modes.

1. Generating the modes with the actual, time-dependent, properties of the constituents leads to the most accurate model, both for the overall response of the composite, the average response of the phases and the distribution of the fields, independently of the evolution of the contrast between the phases.
2. When the time history of the material properties is not available, but the initial and final states of the constituents are known, the most accurate predictions at the same three levels (effective, average per phase, local fields) are obtained by merging the initial and the final modes.
3. When the contrast between the phases between the initial and final states is not reversed, accurate predictions for the effective response are obtained with the initial modes. However a more local description of the fields in the phases requires to combine the initial and final modes or to generate them with the actual time-dependent properties of the phases.
4. When the contrast between the phases is reversed, predicting accurately the effective response of the composite requires the initial and final modes. This is even more true for the local response.
5. The best compromise between accuracy and performance is to use the NTFA approach with global modes.

6. General conclusion

The present study has shown the capability of the Non Uniform Transformation Field Analysis to predict the overall response, as well as the distribution of the local fields, in three-phase viscoelastic composites with three-dimensional microstructure. In particular, its ability to handle individual constituents undergoing aging and swelling, in addition to creep, has been demonstrated. This situation is typically encountered in the nuclear fuel MOX under irradiation which has been chosen to illustrate the theory. The NTFA is based on the notion of modes which serve as shape functions for the viscous or transformation strains. Two different models have been investigated:

a) In the first model (global model), the modes are defined on the whole volume element (global modes).

b) In the second model (local model), the modes are identified separately in each individual phase (local modes). This second model was initially proposed by Michel and Suquet (2003, 2004) for *nonlinear* viscous composites.

A first conclusion of this study is that, *in the present context of linear constituents*, the model with global modes is a good compromise between accuracy and cost. Its extension to nonlinear constituents remains widely open.

A second conclusion is that, for aging constituents, the best compromise for the modes is to combine the modes in the initial state of the material with those in the final state of the material.

Acknowledments: J.C. Michel and P. Suquet acknowledge the financial support of the French Commissariat à l'Energie Atomique via grant CEA-EDF-CNRS 038279, of the Labex MEC and of A*Midex through grants ANR-11-LABX-0092 and ANR-11-IDEX-0001-02. R. Largenton acknowledges the financial support of Électricité de France via the COMCRAY project. The authors are indebted to R. Masson and G. Thouvenin for fruitful discussions.

References

Barbero, E., Luciano, R., 1995. Micromechanical formulas for the relaxation tensor of linear viscoelastic composites with transversely isotropic fibers. Int. J. Solids Structures **32**, 1859–1872.

Baron, D., Thevenin, P., Largenton, R., Masson, R., Pujet, S.,Arnaud, R., 2008. CYRANO3 the EDF Fuel Performance code Especially designed for Engineering applications. Proc. Water Reactor Fuel Performance. paper **8032**.

Berkooz, G., Holmes, P., Lumley, J. L., 1993. The proper orthogonal decomposition in the analysis of turbulent flows. Annual Review of Fluid Mechanics **25**, 539–575.

Beurthey, S., Zaoui, A., 2000. Structural morphology and relaxation spectra of viscoelastic heterogeneous materials. Eur. J. Mech. A/Solids **19**, 1–16.

Chaboche, J.-L., Kruch, S., Maire, J., Pottier, T., 2001. Towards a micromechanics based inelastic and damage modeling of composites. Int. J. Plasticity **17**, 411–439.

Chinesta, F., Ammar, A., Leygue, A., Keunings, R., 2011. An overview of the proper generalized decomposition with applications in computational rheology. J. Non-Newtonian Fluid Mech. **166**, 578–592.

Dvorak, G., 1992. Transformation field analysis of inelastic composite materials. Proc. R. Soc. Lond. A **437**, 311–327.

Dvorak, G., Bahei-El-Din, Y., Wafa, A., 1994. The modeling of inelastic composite materials with the transformation field analysis. Modelling Simul. Mater. Sci. Eng **2**, 571–586.

Feyel, F., 1999. Multiscale FE^2 elastoviscoplastic analysis of composite structures. Comput. Mater. Sc. **16**, 344–354.

Feyel, F., Chaboche, J.-L., 2000. FE^2 multiscale approach for modelling the elastoviscoplastic behaviour of long fibre SiC/Ti composite materials. Computer Methods in Applied Mechanical Engineering **183**, 309–330.

Fish, J., Shek, K., Pandheeradi, M., Shepard, M., 1997. Computational plasticity for composite structures based on mathematical homogenization: Theory and practice. Comput. Methods Appl. Mech. Engrg. **148**, 53–73.

Fish, J., Yu, Q., 2002. Computational Mechanics of Fatigue and Life Predictions for Composite Materials and Structures. Comput. Methods Appl. Mech. Engrg. **191**, 4827–4849.

Fritzen, F., Böhlke, T., 2010. Three-dimensional finite element implementation of the nonuniform transformation field analysis. International Journal for Numerical Methods in Engineering **84**, 803–829.

Fritzen, F., Böhlke, T., 2013. Reduced basis homogenization of viscoelastic composites. Composites Science and Technology 76, 84–91.

González, C., Llorca, J., 2007. Virtual fracture testing of composites: A computational micromechanics approach. Engineering Fracture Mechanics **74**, 1126–1138.

Hashin, Z., 1965. Viscoelastic behavior of heterogeneous media. J. Appl. Mech. **32**, 630–636.

Holmes, P. J., Lumley, J. L., Berkooz, G., 1996. Structures, Dynamical Systems and Symmetry. Cambridge University Press, Cambridge.

Kattan, P., Voyiadjis, G., 1993. Overall damage and elastoplastic deformation in fibrous metal matrix composites. Int. J. Plasticity **9**, 931–949.

Kowalczyk-Gajewska, K., Petryk, H., 2011. Sequential linearization method for viscous/elastic heterogeneous materials. Eur. J. Mech.-A/Solids **30** (5), 650–664.

Ladeveze, P., Passieux, J. C., Neron, D., 2010. The LATIN multiscale computational method and the proper orthogonal decomposition. Computer Methods in Applied Mechanics and Engineering **199**, 1287–1296.

Lahellec, N., Suquet, P., 2007. Effective behavior of linear vicoelastic composites: a time-integration approach. Int. J. Sol. Struct. **44**, 507–529, doi:10.1016/j.ijsolstr.2006.04.038.

Lahellec, N., Suquet, P., 2013. Effective response and field statistics in elasto-(viscoplastic) composites under radial and non-radial loadings. Int. J. Plasticity **40**, 1–30.

Largenton, R., Blanc, V., Thevenin, P., Baron, D., 2010. Simulation and modelling the heterogeneous effects of microstructure mox fuels on their effective properties in nominal pressure water reactor conditions. Advances in Science and Technology **73**, 91–96. doi:10.4028/www.scientific.net/AST.73.91

Laws, N., Mc Laughlin, R., 1978. Self-consistent estimates for the viscoelastic creep compliance of composite materials. Proc. R. Soc. London A **359**, 251–273.

Lee, H., Brandyberry, M., Tudor, A., and Matous K., Three-dimensional reconstruction of statistically optimal unit cells of polydisperse particulate composites from microtomography, Physical Review E, 80(6), 061301-1 061301-12.

Masson, R., Brenner, R., Castelnau, O., 2012. Incremental homogenization approach for ageing viscoelastic polycrystals. C. R. Mécanique **340**, 378–386.

Michel, J.-C., Galvanetto, U., Suquet, P., 2000. Constitutive relations involving internal variables based on a micromechanical analysis. In: Maugin, G., Drouot, R., Sidoroff, F. (Eds.), Continuum Thermomechanics: The Art and Science of Modelling Material Behaviour. Klüwer Acad. Pub., pp. 301–312.

Michel, J.-C., Moulinec, H., Suquet, P., 1999. Effective properties of composite materials with periodic microstructure: a computational approach. Comp. Meth. Appl. Mech. Engng. **172**, 109–143.

Michel, J.-C., Suquet, P., 2003. Nonuniform Transformation Field Analysis. Int. J. Solids Structures **40**, 6937–6955, doi:10.1016/S0020-7683(03)00346-9.

Michel, J.-C., Suquet, P., 2004. Computational analysis of nonlinear composite structures using the Nonuniform Transformation Field Analysis. Comp. Meth. Appl. Mech. Engrg. **193**, 5477–5502.

Michel, J.-C., Suquet, P., 2009. Nonuniform Transformation Field Analysis: a reduced model for multiscale nonlinear problems in Solid Mechanics. In: Aliabadi, F., Galvanetto, U. (Eds.), Multiscale Modelling in Solid Mechanics – Computational Approaches. Imperial College Press, pp. 159–206, chapter 4.

Oudinet, G., Munoz-Viallard, I., Aufore, L., Gotta, M.-J., Becker, J.-M., Chiarelli, G.,Castelli, R., 2008. Characterization of plutonium distribution in MIMAS MOX by image analysis. Journal of Nuclear Materials **375**, 86–94, doi:10.1016/j.jnucmat.2007.10.013.

Rekik, A., Brenner, R., 2011. Optimization of the collocation inversion method for the linear viscoelastic homogenization. Mech. Res. Comm. **38**, 305–308.

Ricaud, J.-M., Masson, R., 2009. Effective properties of linear viscoelastic heterogeneous media: Internal variables formulation and extension to ageing behaviours. Int. J. Solids Structures **46**, 1599–1606.

Rougier, Y., Stolz, C., Zaoui, A., 1993. Représentation spectrale en viscoélasticité linéaire des matériaux hétérogènes. C.R. Acad. Sc. Paris, II **316**, 1517–1522.

Saltykov S. A., 1970, Stereometric Metallography. Metallurgy. Moscow.

Sanchez-Hubert, J., Sanchez-Palencia, E., 1978. Sur certains problèmes physiques d'homogénéisation donnant lieu à des phénomènes de relaxation. C.R. Acad. Sc. Paris Série A **286**, 903–906.

SCDAP RELAP5, Development Team., 1997. A library of materials properties for light water reactor accident analysis. In: SCDAP RELAP5 MOD3.2, Code Manual. Vol. **4**. NUREG CR-6150, INEL-96 0422, pp. 2-70–2-84.

Sirovich, L., 1987. Turbulence and the dynamics of coherent structures. Quarterly of Applied Mathematics **45**, 561–590.

Suquet, P., 1987. Elements of Homogenization for Inelastic Solid Mechanics. In: Sanchez-Palencia, E., Zaoui, A. (Eds.), Homogenization Techniques for Composite Media. Vol. **272** of Lecture Notes in Physics. Springer Verlag, New York, pp. 193–278.

Suquet, P., 1997. Effective properties of nonlinear composites. In: Suquet, P. (Ed.), Continuum Micromechanics. Vol. **377** of CISM Lecture Notes. Springer Verlag, New York, pp. 197–264.

Vu, Q. H., Brenner, R., Castelnau, O., Moulinec, H., Suquet, P., 2012. A self-consistent estimate for linear viscoelastic polycrystals with internal variables inferred from the collocation method. Modell. Simul. Mater. Sci. Eng. **20**, 024003.

Yi, Y., Park, S., Youn, S., 1998. Asymptotic homogenization of voiscoelastic composites with periodic microstructure. Int. J. Solids Structures **35**, 2039–2055.

Zohdi, T. I., Wriggers, P., 2005. Introduction To Computational Micromechanics. Vol. 20 of Lecture Notes in Applied and Computational Mechanics. Springer-Verlag, Berlin.

Appendix A. Representativity of the volume element

Results of full-field simulations performed on 8 different realizations of the microstructure are reported and compared in this appendix. The aim of this comparison is first to obtain reference results for the reduced models (section 4), second to assess the variability of the full-field results when different realizations are considered.

Appendix A.1. Different realizations

Eight realizations of the three-phase volume element have been generated with the same statistical data namely 15% in volume fraction of Pu clusters with diameter in the range $[10\mu m, 70\mu m]$ and 25% in volume fraction of U clusters. More specifically the unit-cell is a cube with size $(150\mu\text{m})^3$, each realization contains a total of 121 Pu inclusions, namely 97 inclusions with a diameter of 10μm, 16 inclusions with diameter of 20μm, 3 inclusions with a diameter of 30μm, 3 inclusions with a diameter of 40μm, 1 inclusion with a diameter of 50μm and 1 inclusion with a diameter of 70μm and 57 U inclusions with a diameter of 30μm.

The variablity in the realizations comes from the position of the inclusions which are randomly located (under the only constraint of non overlapping) and vary from one realization to another. The first realization is the one shown in Figure 2. (Fig. A.20). In order to investigate the sensitivity of the reponse of the composite to the choice of the microstructure, all realizations are subjected to the first loading case (20), namely tension-torsion at constant strain-rate with swelling. The constitutive relations of the phases are given in section 2.2. Two cases where considered, with or without aging of the phases. In the non-aging case, the material data are taken from Table 1. In the aging case, the material data are that of section 5.3, with $\zeta = 0.1865$ with inversion of the contrast of the viscosity between the matrix and the Pu inclusions. The reader is referred to section 5.3 and to Appendix C for more details about the variations in time of the viscosity of the phases.

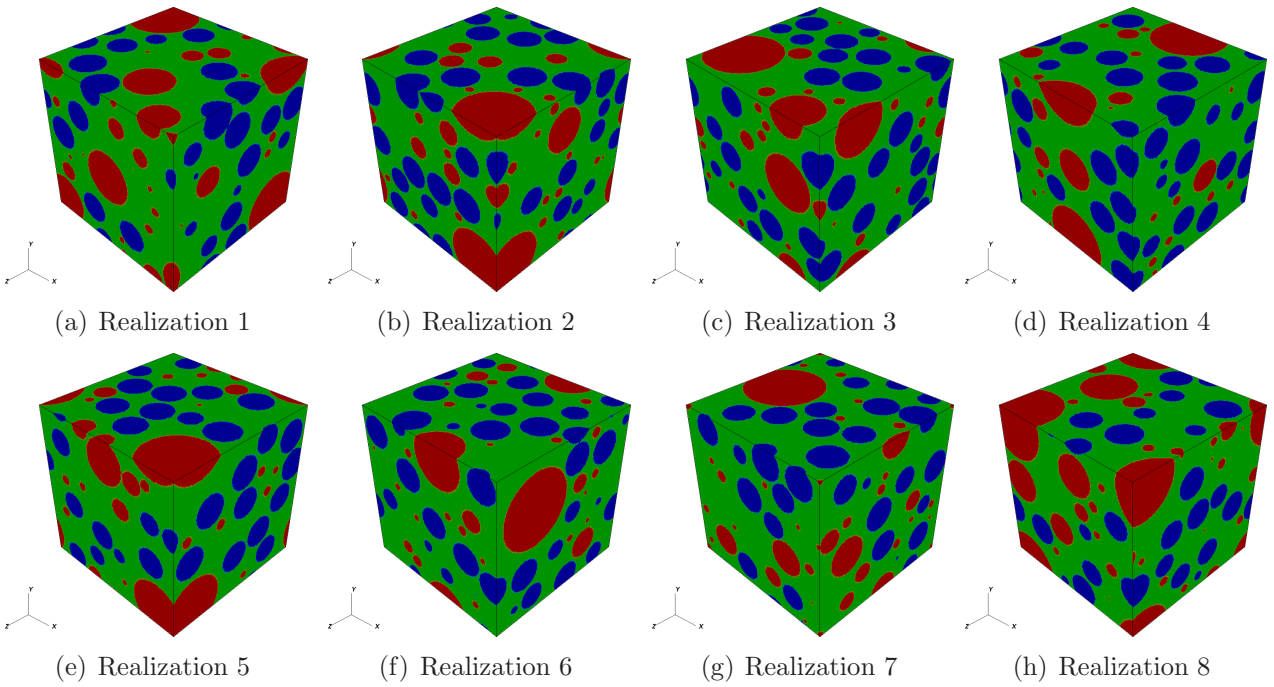

(a) Realization 1 (b) Realization 2 (c) Realization 3 (d) Realization 4

(e) Realization 5 (f) Realization 6 (g) Realization 7 (h) Realization 8

Figure A.20: Three-phase composites with polydisperse inclusions. Eight different periodic realizations.

When the phases are non-aging, the effective response, the average response of the individual phases and the distribution of the local stress in the phases are shown in Figure A.21. The effective response of the 8 realizations are very close to each other. Therefore the characteristics of the volume element (number and size of the inclusions compared to the size of the cube) are sufficient to approach the effective response with a good accuracy. The size of this volume element is 150 μm, which is small compared to the size of the MOX pellet (4.0 mm). However the ratio between the size of the volume element and the largest inclusion (70 μm) is about 2.14. Figure A.21(a) shows that even if this ratio is not very large, it is sufficient to attain stationarity of the effective properties. However, this does not guarantee stationarity of other properties, such as the field distribution. Therefore the average the intensity of the stress over each individual constituent is also shown in Figure A.21(b) for the 8 different realizations. The intensity is defined as $(\sigma_{ij}\sigma_{ij})^{1/2}$. Again the curves in each constituent show little dispersion, except in the U clusters where the difference between the min and max values can reach 6.0 % of the average stress. This discrepancy remains acceptable. Moreover the deviation from the mean value over the 8 realizations is less than 4 % for the first realization which will be retained to generate the NTFA modes. Given the small discrepancy, the size of the volume element can also be considered as sufficient to deliver a representative response for the averages of the fields over each phase. Finally the distribution of the local fields has been investigated and shown in figure A.21(c). The standard deviation from the average does not exceed 13.0% and is maximal in the U clusters. For the first realization, which has been chosen for implementation of the NTFA, this deviation is less than 8 %.

When the phases are aging, the deviations among the eight representative cell realizations of materials exhibiting swelling and aging are similar to that observed in the previous cases of non-aging phases (see figure A.22).

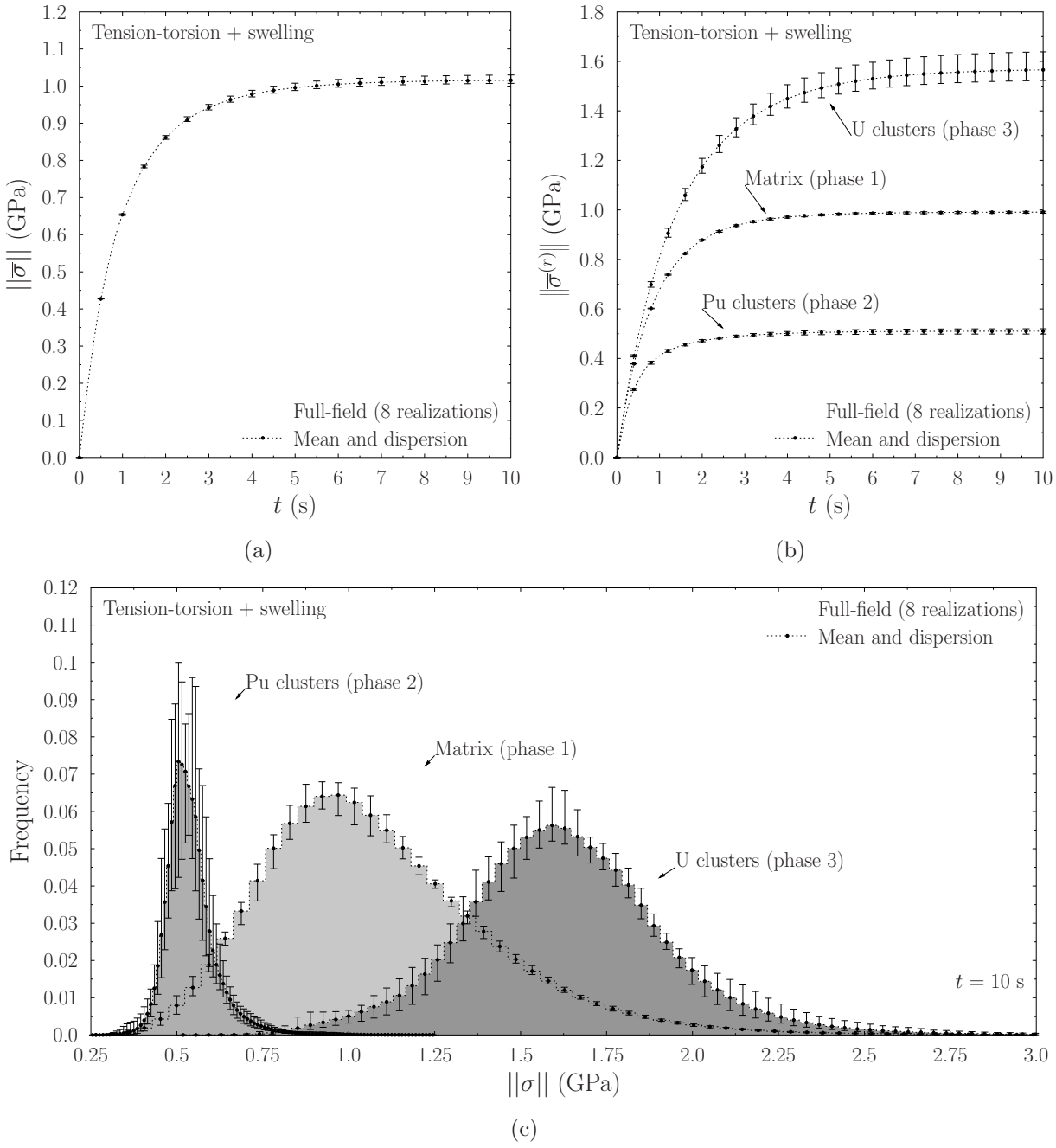

Figure A.21: Non-aging constituents. Tension-torsion test at constant strain-rate with swelling. (a): Effective response. (b): Average stress in the individual phases. Mean and dispersion. (c) Probability distribution of the stress in the different phases.

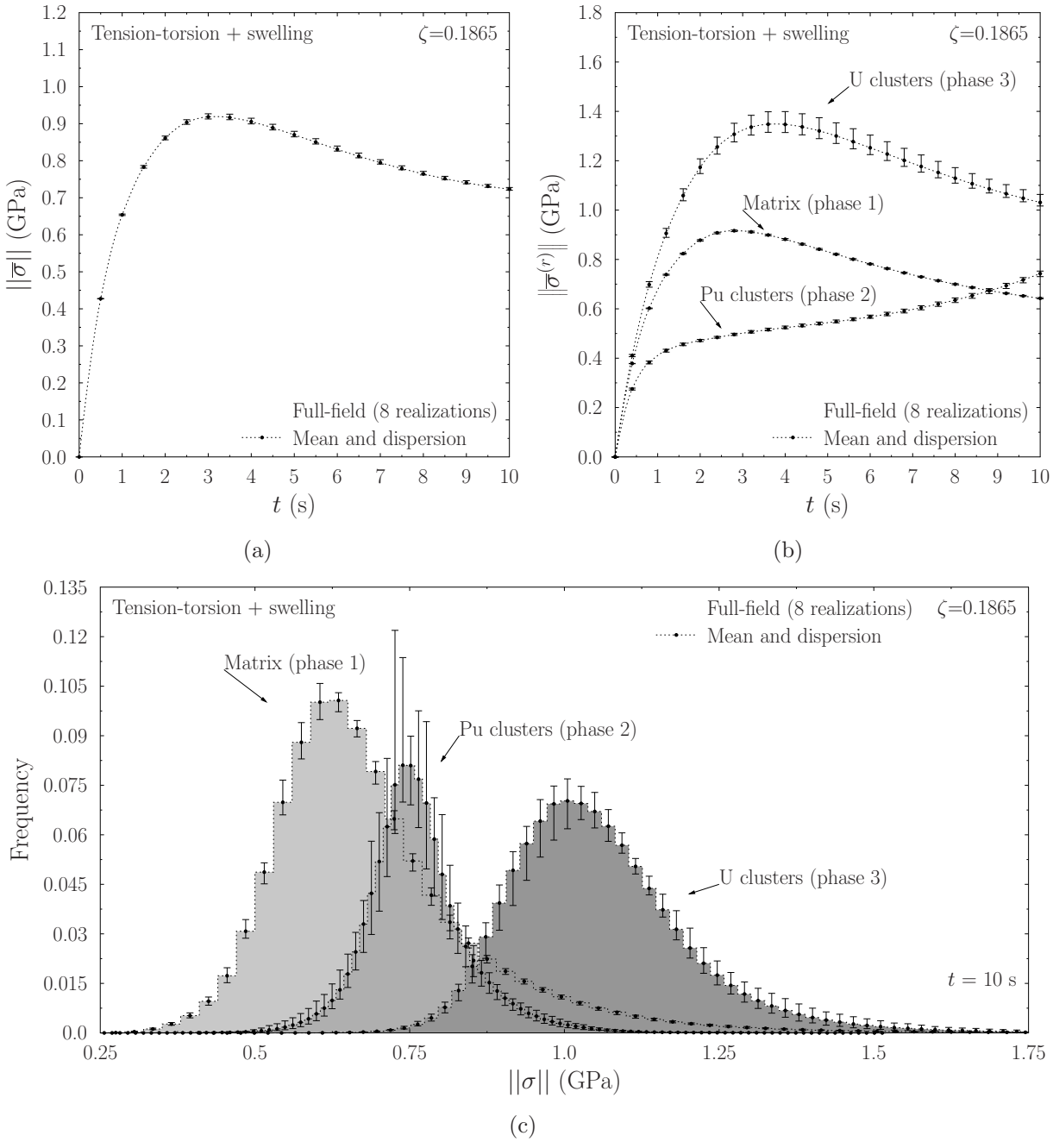

Figure A.22: Aging constituents. Tension-torsion test at constant strain-rate with swelling. (a): Effective response. (b): Average stress in the individual phases. Mean and dispersion. (c) Probability distribution of the stress in the different phases.

Appendix B. A priori elastic computations required by the NTFA

The implementation of the NTFA requires to solve *once for all* a few elastic problems to determine the tensor field $\boldsymbol{A}$ and $\boldsymbol{D}$ entering (7) and from which other quantities of interest can be deduced (see (10)).

Appendix B.1. Elastic localization

The elastic localization tensor $\boldsymbol{A}$ is obtained by solving 6 elasticity problems in the form

$$\left.\begin{array}{c} \operatorname{div}(\boldsymbol{\sigma}(\boldsymbol{x}))=0, \quad \boldsymbol{\varepsilon}(\boldsymbol{x})=\frac{1}{2}\left(\boldsymbol{\nabla u}+\boldsymbol{\nabla u}^{\mathsf{T}}\right), \\ \boldsymbol{\sigma}(\boldsymbol{x})=\boldsymbol{L}(\boldsymbol{x}):\boldsymbol{\varepsilon}(\boldsymbol{x}), \quad \boldsymbol{u}-\overline{\boldsymbol{\varepsilon}}.\boldsymbol{x}\ \#, \quad \boldsymbol{\sigma}.\boldsymbol{n}\ -\# \end{array}\right\} \tag{B.1}$$

where $\overline{\boldsymbol{\varepsilon}}$ is successively prescribed to the 6 elementary strain states $\boldsymbol{i}^{(ij)}$

$$i_{kh}^{(ij)}=\frac{1}{2}\left(\delta_{ik}\delta_{jh}+\delta_{ih}\delta_{jk}\right),$$

(δ being the *Kronecker* symbol). Let $\boldsymbol{u}^{(kh)}$ be the displacement field solution of (B.1) when $\overline{\boldsymbol{\varepsilon}}=\boldsymbol{i}^{(kh)}$. Then the localization tensor $\boldsymbol{A}$ reads as:

$$A_{ijkh}(\boldsymbol{x})=\varepsilon_{ij}(u^{(kh)}(\boldsymbol{x})). \tag{B.2}$$

Once $\boldsymbol{A}$ is determined, the 4-th order effective stiffness tensor $\widetilde{\boldsymbol{L}}$ and the 2nd-order tensor $\boldsymbol{a}_k$ in (10) are obtained as:

$$\widetilde{\boldsymbol{L}}=\langle \boldsymbol{L}:\boldsymbol{A}\rangle=\langle \boldsymbol{A}^{\mathsf{T}}:\boldsymbol{L}:\boldsymbol{A}\rangle, \quad \boldsymbol{a}_k=\langle \boldsymbol{\mu}^k:\boldsymbol{L}:\boldsymbol{A}\rangle.$$

Appendix B.2. Influence tensors

By definition $\boldsymbol{D}*\boldsymbol{\mu}$ is the strain field created by an eigenstrain field $\boldsymbol{\mu}$ under a vanishing overall deformation. It solves the following thermoelastic problem (interpreting $\boldsymbol{\mu}$ as a thermal strain field)

$$\left.\begin{array}{c} \operatorname{div}(\boldsymbol{\sigma}(\boldsymbol{x}))=0, \quad \boldsymbol{\varepsilon}(\boldsymbol{x})=\frac{1}{2}\left(\boldsymbol{\nabla u}+\boldsymbol{\nabla u}^{\mathsf{T}}\right), \\ \boldsymbol{\sigma}(\boldsymbol{x})=\boldsymbol{L}(\boldsymbol{x}):\left(\boldsymbol{\varepsilon}(\boldsymbol{x})-\boldsymbol{\mu}(\boldsymbol{x})\right), \quad \boldsymbol{u}-\overline{\boldsymbol{\varepsilon}}.\boldsymbol{x}\ \#, \quad \boldsymbol{\sigma}.\boldsymbol{n}\ -\# \end{array}\right\} \tag{B.3}$$

$\boldsymbol{D}*\boldsymbol{\mu}^k(\boldsymbol{x})$ and $\boldsymbol{D}*\chi^{(r)}\boldsymbol{i}$ are solution of the thermoelastic problem (B.3) with $\boldsymbol{\mu}=\boldsymbol{\mu}^k$ and $\boldsymbol{\mu}=\chi^r\boldsymbol{i}$ respectively. The stress field $\boldsymbol{\rho}^k$ and $\boldsymbol{\xi}^r$ are the corresponding stress fields.

Appendix C. Aging constituents. Variations of the phase viscosity with time

The variations of the fluidity (inverse of the viscosity) of the matrix with respect to time are assumed to be bilinear, with a first linear ramp from 0 to $t^{(1)}$ and a second ramp from $t^{(1)}$ to the final time T. These variations, obtained by a neutron model implemented in the

nuclear fuel code Cyrano3 (Baron et al., 2008), are better expressed by comparing the value of the viscosity at time t with its initial value at time $t = 0$:

$$\frac{G_{\mathsf{v}}^{(1)}(0)}{G_{\mathsf{v}}^{(1)}(t)} = \begin{cases} 1 + \theta^{(1)} t, \quad 0 \le t \le t^{(1)}, \\ (1 + \theta^{(1)} t^{(1)}) + \left(\dfrac{T - t}{T - t^{(1)}} \right) + \dfrac{G_{\mathsf{v}}^{(1)}(0)}{G_{\mathsf{v}}^{(1)}(T)} \left(\dfrac{t - t^{(1)}}{T - t^{(1)}} \right), \quad t^{(1)} \le t \le T. \end{cases}$$

The plots shown in Figure 11 correspond to the following data:

$$t^{(1)} = 2 \text{ s}, \quad T = 10 \text{ s}, \quad \theta^{(1)} = 0.38969\ 10^{-3}, \quad \frac{G_{\mathsf{v}}^{(1)}(0)}{G_{\mathsf{v}}^{(1)}(T)} = 1.78. \tag{C.1}$$

Similarly the fluidity in the Pu clusters is governed by

$$\frac{G_{\mathsf{v}}^{(2)}(0)}{G_{\mathsf{v}}^{(2)}(t)} = \begin{cases} 1 + \theta^{(2)} t, \quad 0 \le t \le t^{(1)} \\ (1 + \theta^{(2)} t^{(1)}) \left(\dfrac{T - t}{T - t^{(1)}} \right) + \dfrac{G_{\mathsf{v}}^{(2)}(0)}{G_{\mathsf{v}}^{(2)}(T)} \left(\dfrac{t - t^{(1)}}{T - t^{(1)}} \right), \quad t^{(1)} \le t \le T. \end{cases}$$

with

$$\theta^{(2)} = \frac{\zeta \frac{G_{\mathsf{v}}^{(1)}(0)}{G_{\mathsf{v}}^{(1)}(T)} - 1}{\frac{G_{\mathsf{v}}^{(1)}(0)}{G_{\mathsf{v}}^{(1)}(T)} - 1} \theta^{(1)}, \quad \zeta = \left(\frac{G_{\mathsf{v}}^{(2)}(0)}{G_{\mathsf{v}}^{(2)}(T)} \right) / \left(\frac{G_{\mathsf{v}}^{(1)}(0)}{G_{\mathsf{v}}^{(1)}(T)} \right).$$

ζ is the parameter which controls the contrast of viscosity between the Pu clusters and the matrix. When $\zeta = 1$, the two viscosities have the same time dependence (see Figure 11 where for $\zeta = 1$ all viscosity curves are parallel). When $\zeta > 1$ the two curves diverge, whereas they converge when $\zeta < 1$.